Deciphering Colorectal Cancer-Hepatocyte Interactions: A Multiomic Platform for Interrogation of Metabolic Crosstalk in the Liver-Tumor Microenvironment

Alisa B. Nelson[1], Lyndsay E. Reese[2], Elizabeth Rono[3], Eric D. Queathem[1,4,5], Yinjie Qiu[6], Braedan M. McCluskey[6], Alexandra Crampton[3], Eric Conniff[3], Katherine Cummins[3], Ella Boytim[7], Senali Dansou[3], Justin Hwang[7], Sandra Safo[8], Patrycja Puchalska[1], David K. Wood[3], Kathryn L. Schwertfeger[2,7], Peter A. Crawford[1,3*]

[1]Division of Molecular Medicine, Department of Medicine, University of Minnesota, Minneapolis, MN USA;
[2]Department of Laboratory Medicine and Pathology, University of Minnesota, Minneapolis, MN USA;
[3]Department of Biomedical Engineering, University of Minnesota, Minneapolis, MN USA;
[4]Department of Biochemistry, Molecular Biology, and Biophysics, University of Minnesota, Minneapolis, MN USA;
[5]Department of Integrative Biology and Physiology, University of Minnesota Medical School, Minneapolis, MN, USA;
[6]Minnesota Supercomputing Institute, Minneapolis, MN USA;
[7]Masonic Cancer Center, University of Minnesota, Minneapolis, MN USA;
[8]Division of Biostatistics and Health Data Science, University of Minnesota, Minneapolis, MN, USA

*Corresponding author

Email: crawforp@umn.edu

Author Contributions: ABN, LER, ER, AC, EC, KC, PP, DKW, KLS, PAC: conception and design of the experiments. ABN, LER, EDQ, YQ, BMM, EB, SD, JH, PP, DKW, KLS, PAC: collection, analysis, and interpretation of data. ABN, PP, DKW, KLS, PAC: drafting and revising the manuscript. DKW, KLS, PAC: funding acquisition. All authors have read and approved the final submission.

Competing Interest Statement: P.A.C. has served as an external consultant for Pfizer, Inc., Abbott Laboratories, Janssen Research & Development and Juvenescence. A.C. is now an employee of Solventum.

Keywords: Cancer metabolism, metabolomics, multi-omics, tumor microenvironment

Abstract

Metabolic reprogramming is a hallmark of cancer, enabling tumor cells to adapt to and exploit their microenvironment for sustained growth. The liver is a common site of metastasis, but the interactions between tumor cells and hepatocytes remain poorly understood. In the context of liver metastasis, these interactions play a crucial role in promoting tumor survival and progression. This study leverages multiomics coverage of the microenvironment via liquid chromatography and high-resolution, high-mass accuracy mass spectrometry-based untargeted metabolomics, ^{13}C-stable isotope tracing, and RNA sequencing to uncover the metabolic impact of co-localized primary hepatocytes and a colon adenocarcinoma cell line, SW480, using a 2D co-culture model. Metabolic profiling revealed disrupted Warburg metabolism with an 80% decrease in glucose consumption and 94% decrease in lactate production by hepatocyte-SW480 co-cultures relative to SW480 control cultures. Decreased glucose consumption was coupled with alterations in glutamine and ketone body metabolism, suggesting a possible fuel switch upon co-culturing. Further, integrated multiomic analysis indicates that disruptions in metabolic pathways, including nucleoside biosynthesis, amino acids, and TCA cycle, correlate with altered SW480 transcriptional profiles and highlight the importance of redox homeostasis in tumor adaptation. Finally, these findings were replicated in 3-dimensional microtissue organoids. Taken together, these studies support a bioinformatic approach to study metabolic crosstalk and discovery of potential therapeutic targets in preclinical models of the tumor microenvironment.

Introduction

The liver is the site of one of six cancers with increasing incidence of primary tumors – hepatocellular carcinoma (hepatoma) (1). Moreover, the liver is a common site of solid tumor cell metastasis, including from breast and colorectal cancers, causing significant morbidity and mortality (2). Tumor cells within the liver interact with liver resident cell types, including hepatocytes. Metabolic adaptation is essential for tumor success throughout cancer cell transformation, proliferation, and metastasis (3, 4). Cancer cells reprogram their metabolism to meet increased demands for energy, biosynthesis, and redox homeostasis. Studies show this adaptation extends to the tumor microenvironment where cancer cells can tune and exploit their environment to meet metabolic needs (5-8). Within the liver, hepatocytes engage dynamic metabolic programs to support local and systemic physiology. Exploitation of this rich metabolic environment may represent an essential interaction that facilitates tumor cell colonization in the liver niche. However, our understanding of the specific interactions between cancer cells and hepatocytes that drive survival and proliferation in the metastatic liver niche remains limited. Previous studies profiling metabolism of HCC indicates transformed hepatocytes engage in aerobic glycolysis and altered lipid and amino acid metabolism (9, 10). Moreover, substrate fuels are used to program neighboring immune cells for repressed anti-tumor responses (7). Metastasizing cells have been shown to require adaptations that help them overcome the hypoxic liver microenvironment (11-13). But these studies do not consider the role of co-localized, non-transformed hepatocytes. Additionally, these studies are limited in their coverage of the omics landscape.

45 Metabolomics technologies are well-positioned to reveal potential metabolic adaptation
46 in cancer. Mass spectrometry-based untargeted metabolomics surveys global metabolic
47 shifts among samples by measuring the fluctuations of multiple chemical feature
48 abundances detected as mass-to-charge (*m/z*) signal and retention time pairs (14-16). An
49 additional dimension of information can be gained by the convergent use of ^{13}C-labeled
50 stable isotope tracers. While static measurement of metabolites provides a snapshot of
51 perturbed influxes or effluxes that lead toward or away from measured metabolites, these
52 measurements often fail to reveal nodes through which shifts occur without significant fold
53 changes in the static abundance of metabolites (17). Merging the advantages of high-
54 resolution mass spectrometry-based untargeted metabolomics with ^{13}C-stable isotope
55 labeling known as isotope tracing untargeted metabolomics (ITUM) provides a unique
56 opportunity to discover dynamic and potentially crucial metabolic pathways (18-21).
57 However, studying metabolic communication in the microenvironment is an ongoing
58 challenge (22). Stable isotopes present an advantage, but developing model systems
59 amenable to ITUM approaches while maintaining physiological relevance is difficult. Here,
60 we present an approach using our untargeted metabolomics and ITUM pipelines in an
61 engineered *in vitro* model to discover metabolic interactions between colon
62 adenocarcinoma cells (SW480 cell line) and primary hepatocytes. To adapt our pipeline to a
63 mixed cell model, we quantify extracellular and intracellular metabolite pools upon co-
64 culture to identify impacted metabolic pathways. Additionally, we hypothesized that the
65 combined study of differential glucose utilization and metabolite-metabolite relationships
66 could reveal tumor cell metabolic adaptation in the hepatocyte-SW480 microenvironment.

67 Therefore, we present approaches that extend the application of untargeted metabolomics
68 and ITUM to reveal nodes of adaptation in the tumor-hepatocyte microenvironment. Finally,
69 a multiomic integration with the transcriptome links metabolic adaptations to altered
70 functional programs in tumor cells with co-localized hepatocytes.
71
72 **Results**
73 **Co-culture of SW480 cells with primary hepatocytes reprograms metabolism.** We used
74 a co-culture model to study metabolic adaptation of tumor cells to the hepatocyte
75 microenvironment. Culturing primary hepatocytes is challenged by their loss of hepatocyte-
76 like function through de-differentiation (23, 24). However, co-culture with 3T3-J2 murine
77 embryonic fibroblasts can sustain hepatocellular function for more than 6 weeks (25).
78 Therefore, we directly co-cultured primary rat hepatocytes, murine 3T3-J2 fibroblasts (J2s),
79 and the human colon adenocarcinoma cell line, SW480 (**Figure 1A**). To form 2D co-cultures,
80 J2s were growth arrested and then plated with hepatocytes in 12-well plates to sustain
81 hepatocellular function (HJ cultures). Control plates of J2s were plated on the same day in
82 preparation for SW480-J2 (SJ) control co-cultures. After 7 days, SW480s were seeded to form
83 SW480-J2-Hepatocyte (SJH) co-cultures and SJ controls. All media and cells were collected
84 on day 10 for metabolomics and transcriptomics analyses (**Figure 1B**). In each experiment,
85 the group of interest, SJH, was compared to HJ and SJ controls.
86 Cancer metabolism is hallmarked by high glucose consumption and utilization through
87 aerobic glycolysis, resulting in high lactate production, known as the Warburg Effect (26, 27).
88 Hepatocytes play significant roles in regulating glucose homeostasis. We hypothesized that

89 hepatocytes may impact glucose metabolism in co-cultures. Therefore, we quantified net
90 changes in glucose and lactate concentrations in conditioned cell culture media using ^{1}H-
91 nuclear magnetic resonance (NMR) spectroscopy. Then, we normalized changes in
92 exogenous metabolite concentrations to cellular biomass (DNA content) to report net
93 glucose consumption and lactate production over 24 hours. As expected, SJ controls model
94 the Warburg effect in culture, consuming 2.50 ± 0.01 mol glucose/day/mg DNA, and
95 producing 3.86 ± 0.05 mol lactate/day/mg DNA (**Figure 2A**). The presence of hepatocytes
96 decreased total glucose consumption by 80% (0.5 ± 0.05 mol glucose/day/mg DNA) and
97 lactate production by 94% to 0.23 ± 0.01 mol lactate/day/mg DNA. Furthermore, the ratio of
98 lactate to glucose significantly decreased from 1.54 ± 0.02 to 0.46 ± 0.05, suggesting the
99 presence of hepatocytes disrupts Warburg metabolism of SW480s (**Figure 2B**).

100 To determine if decreased utilization of glucose by SW480 cells when co-cultured with
101 hepatocytes could result from a fuel switch from glucose to other available substrates, we
102 quantified hepatocyte-derived ketones and culture media-derived glutamine. Using a
103 UHPLC-MS/MS based approach, we quantified total ketone bodies in the conditioned media
104 of co-cultures after 24 hours. As expected, primary rat hepatocyte control co-cultures
105 produced the ketone bodies acetoacetate (AcAc) and β-hydroxybutyrate (βOHB, **Figure 2C**).
106 In the presence of SW480s, total ketone bodies recovered in the media were diminished by
107 64%, suggesting either decreased production by hepatocytes or increased consumption of
108 ketones by non-hepatocyte cells. Glutamine abundance was also significantly decreased in
109 SJH co-cultures relative to both HJ and SJ controls (**Figure 2D**). Interestingly, glutamine
110 abundance decreased 36% in SJH relative to SJ controls, suggesting the presence of

111 hepatocytes further enhanced glutamine dependence of SW480s. Together these data
112 suggest an adaptation to fuel utilization in hepatocyte-SW480 co-cultures.

113 To survey metabolic interaction-dependent metabolite shifts resulting from co-culture,
114 we next used differential analysis of features detected by LC-MS-based label-free
115 untargeted metabolomics. Prior to any downstream analysis, low variance features were
116 removed, features of interest were annotated in Compound Discoverer 3.3, and when
117 possible, matched to commercial standards and MS/MS spectral libraries. Five metabolic
118 features by LC-MS-based untargeted profiling increased more than 2-fold ($\log_2 \geq 1$) in SJH
119 compared to HJ controls. This included putative S-adenosylhomocysteine (SAH; **Table 1,**
120 **Figure 2E**), an intermediate of one-carbon metabolism. Compared to HJ, SJH co-cultures
121 showed 142 downregulated features, including pyruvate (**Supplemental Figure 1A**), acetyl-
122 CoA (**Supplemental Figure 1B**), and propionyl-CoA (**Supplemental Figure 1C**), metabolites
123 important in glucose metabolism and the TCA cycle. Relative to SJ controls, SJH co-cultures
124 show a greater than 2-fold increase in 10 features, including propionyl-CoA (**Figure 2F;**
125 **Supplemental Figure 1C**), glutamyl-glycine, an intermediate of glutathione metabolism,
126 and acetyl-CoA (**Supplemental Figure 1B**). A ≥2-fold decrease was observed in 119 features
127 in SJH compared to SJ controls, including pyruvate (**Supplemental Figure 1A**), lactate
128 (**Supplemental Figure 1D**), NAD^+ (**Supplemental Figure 1E**), and ATP (**Supplemental**
129 **Figure 1F**). However, decreases in the NAD^+ pool did not lead to a significant change in the
130 NAD^+/NADH ratio in SJH relative to SJ (**Supplemental Figure 1G**). Finally, we calculated
131 energy charge to determine the current energy status of the co-culture based on relative
132 abundance of AMP, ADP, and ATP pools. We saw a modest, but not statistically significant,

133 decrease in SJH relative to SJ co-cultures, suggesting a possible decrease in available energy
134 (**Supplemental Figure 1H-I**).
135 Untargeted metabolomics of mixed cell populations represent metabolite pools that are
136 combined across all cell types. Therefore, changes in relative abundance may represent an
137 adaptation in one cell type, a combination of adaptations across multiple cell types, or could
138 simply be a product of dilution of the pool after adding biomass. Due to the observed number
139 of features that were significantly decreased in SJH relative to either HJ or SJ controls, we
140 sought to determine if our approach detects true biological interactions in hepatocyte and
141 SW480 co-cultures, rather than simple dilutions of HJ or SJ metabolite pools. Therefore, we
142 implemented a dilution approach to identify those features that were significantly different
143 from a HJ-SJ dilution (**Figure 3A**). HJ and SJ extracts were combined 1:1 (1T1) prior to LC-MS
144 injection, alongside HJ, SJ, and SJH samples. Putative metabolites with pool sizes that
145 significantly differed between SJH and controls were compared to the 1T1 dilution sample.
146 A low threshold for discovery was used ($p < 0.05$) to identify those features that may indicate
147 metabolic interactions. Lactate was significantly decreased in SJH relative to 1T1 samples
148 (**Figure 3B; Table 2**). Normalized ion counts for each group and the analytical control, 1T1,
149 are shown in **Supplemental Figure 2**, demonstrating a likely metabolic interaction between
150 SW480s and hepatocytes beyond an outcome that could be explained by simple metabolite
151 pool dilution. Additionally, four glutamyl peptides – including glutamyl-glycine, as well as
152 uracil, uridine diphosphate (UDP), aspartate, and malate were increased more than 2-fold in
153 SJH relative to 1T1 (**Figure 3B; Table 2**). Employment of an analytical 1T1 dilution of controls

154 for differential analysis of directly co-cultured cells reveals biological derangement of
155 metabolite abundances belonging to glycolytic, amino acid, and nucleoside pathways.
156 **Metabolite exchange of nucleoside intermediates.** Untargeted metabolomics results
157 indicate altered activity in both purine and pyrimidine pathways when SW480s are co-
158 cultured with hepatocytes, whose identities were confirmed by retention time and MS/MS
159 fragmentation match to commercial standards (**Figure 2E-F; Figure 3B**). We hypothesized
160 that the presence of hepatocytes may facilitate adaptation through exchange of purine and
161 pyrimidine intermediates. Therefore, we performed LC-MS-based untargeted metabolomics
162 on cell extracts and media after the first 24 hours of direct co-culture to evaluate fold
163 changes in nucleoside intermediate abundance over time. In all three groups, hypoxanthine,
164 an intermediate of purine metabolism, was depleted comparing starting media (t0) to media
165 harvested after 24 hours, indicating uptake from serum-containing media or conversion to
166 other metabolic products (**Figure 4A, Table 3**). SJH co-cultures had 23% (±3%) greater
167 depletion of hypoxanthine compared to HJ controls and 12% (±4%) less than SJ controls
168 (**Supplemental Figure 3**). Interestingly, hypoxanthine abundance was coupled with
169 diminished extracellular uric acid, the terminal product of purine degradation, in HJ and SJH
170 groups, while SJ controls show an average 809% increase in uric acid (**Figure 4A,**
171 **Supplemental Figure 3**). Hypoxanthine and uric acid are both metabolites that can be found
172 in starting media due to the presence of serum. We further analyzed media under normal
173 culture conditions and in the absence of cells to control for possible spontaneous
174 degradation and observed an accumulation of hypoxanthine and uric acid (9% and 47%,
175 respectively) after 24 hours, suggesting instability of upstream metabolites at 37°C (denoted

176 as dotted lines, **Supplemental Figure 3**). Therefore, these data indicate significant
177 metabolic activity in the purine degradation pathway in SJ controls that is altered by the
178 presence of hepatocytes. To investigate if this impacts intracellular purine intermediates, we
179 measured inosine in cellular extracts. Inosine, an intermediate in the purine salvage
180 pathway, showed a 2-fold increase in hepatocyte-containing cultures while it was modestly
181 diminished in SJ controls after 24 hours (**Figure 4B**). Finally, inosine was uniquely enriched
182 from [U-$^{13}C_6$]glucose in HJ and SJH groups but not detectable in SJ in 3D microtissue
183 organoids (**Figure 4C**). Conversely, the average total ^{13}C-enrichment of HJ and SJH groups
184 was 58.7% (± 1.5%) and 64.7% (± 4.5%) of the total inosine pool. This observation suggests
185 that changes in glucose contribution to inosine pools may be localized to hepatocytes.
186 Together these data suggest the presence of hepatocytes increases purine salvage, rescuing
187 cells from uric acid accumulation.
188 *Pyrimidine metabolism is increased in hepatocytes by co-culture with SW480 cells*.
189 Hepatocytes are a primary source of uridine, an intermediate of pyrimidine metabolism. We
190 hypothesized that altered pyrimidine pools may be a result of newly available uridine from
191 hepatocytes. Therefore, we measured pyrimidine intermediates by LC-MS/MS in media and
192 cell extracts to observe changes in pool sizes over 24 hours compared to starting media. As
193 expected, we observed an accumulation of uridine in the media of hepatocyte-containing
194 co-cultures that was not present in SJ controls (**Figure 4D**). Interestingly, we observed an
195 even greater accumulation of orotic acid, an intermediate of *de novo* pyrimidine
196 biosynthesis (**Table 3**). We did not observe a significant difference between SJH and HJ
197 controls, suggesting these media signals are primarily driven by hepatocytes. However,

198 intracellular pool sizes of pyrimidine metabolites showed greater increases in SJH relative to
199 HJ controls, including carbamoyl aspartate – the product of the rate-limiting step in *de novo*
200 pyrimidine biosynthesis, suggesting the co-localization of hepatocytes and SW480s
201 upregulates the pyrimidine biosynthetic pathway (**Figure 4E**).

202 **Discriminant ^{13}C-ITUM analysis of SJH co-cultures.** ^{13}C-stable isotope tracing of
203 metabolic substrates has been used to detect metabolic adaptation (20, 28). However,
204 incorporation of glucose-derived carbon in diverse metabolic pathways in mammalian cells
205 convolutes biological interpretation of enrichment patterns in complex samples. We
206 hypothesized that informatic integration of co-^{13}C-enriched metabolites elucidates pathway
207 activity. Therefore, we employed univariate and multivariate statistical approaches to
208 characterize glucose utilization in co-culture. SJ and SJH co-cultures were treated with [U-
209 $^{13}C_6$]-glucose for 24 hours on day 9. On day 10, cells were snap frozen for ^{13}C-ITUM and
210 acquired LC-MS data was analyzed for ^{13}C-enriched mass isotopomers (*i.e.,* isotopologues)
211 [M+0, M+1, ..., M+n] to identify nodes of glucose-derived metabolism that differentiate SJH
212 co-cultures from SJ controls. We first used principal components analysis (PCA) to identify
213 isotopologues that discriminate SJH co-cultures from HJ and SJ controls (**Figure 5A**). PC1
214 significantly separated SJH and SJ groups, while PC2 moderately separated SJH from HJ
215 controls. Strong association with PC1 indicated co-^{13}C-enrichment of these metabolites
216 captures the impact of hepatocytes on SW480s. To further investigate adaptations to
217 glucose metabolism after co-culturing hepatocytes on SW480s, we performed a univariate
218 correlation analysis of top contributors to PC1 loadings, including only SJ and SJH ^{13}C-
219 enrichment. We visualized these relationships in a correlation matrix (**Figure 5B;**

220 **Supplemental Figure 4**). A positive correlation between feature pairs indicates co-^{13}C-
221 enrichment of isotopologue pools in response to SW480 co-culture with hepatocytes
222 relative to SW480 alone, while a negative correlation indicates a possible bifurcation of ^{13}C-
223 labeled carbon because of co-culture. As would be expected, fractional enrichment of M+0,
224 the isotopologue indicating no ^{13}C incorporation, of several metabolites, including TCA cycle
225 intermediates, were positively associated with each other and clustered together ("Region
226 1" on **Figure 5B**). These M+0 species show a strong negative correlation with the ^{13}C-
227 enriched isotopologues (species in "Region 2"), *e.g.*, M+0 of Glutamate ("E_M0") versus the
228 incorporation of four ^{13}C atoms ("E_M4"). This is the expected relationship and supports the
229 validity of this analytical framework, which also reveals many unanticipated relationships.
230 For example, the M+6 isotopologue of uridine diphosphate N-acetylglucosamine
231 (UDPGlcNAc, corresponding to the direct incorporation of a labeled glucose molecule into
232 glucosamine), clustered with unenriched (M+0) isotopologues of several metabolites in
233 Region 1 (Red arrow, **Figure 5B**) and negatively correlated with enriched glutathione (*e.g.*,
234 GSH_M3, found in Region 2; Blue arrow). UDPGlcNAc M+6 enrichment decreases in co-
235 culture, while enrichment of GSH increases (relative to the SJ condition), suggesting glucose
236 is redirected from the hexosamine biosynthetic pathway to glutathione synthesis in co-
237 culture (**Supplemental Figure 5**). Region 3 shows a cluster of isotopologues from glycolytic
238 and TCA cycle intermediates with strong co-enrichment. As expected, this includes
239 enriched isotopologues of metabolites in the same pathway, such as glutamate (E_M4), a
240 precursor to GSH (GSH_M4; Yellow arrows, **Figure 5B**). The positive co-enrichment of other
241 TCA cycle intermediates with GSH may meet GSH demand in response to co-culture. Finally,

242 Region 4 shows isotopologues with nominal relationships to each other, suggesting little
243 change in response to co-culture. Together these data indicate ^{13}C-enrichment of
244 glutathione from glucose is significantly impacted by co-culturing of SW480s and
245 hepatocytes. Glutathione is an important metabolite in redox homeostasis within the cell
246 and changes to its biosynthesis may be a significant adaptation of metabolic pathways to
247 the tumor-hepatocyte microenvironment.

248 **Transcriptomic analysis of 3-dimensional hepatocyte-SW480 microtissue organoids.** To
249 evaluate SW480 adaptation to co-culturing with hepatocytes in a more physiological setting,
250 we also performed transcriptomic profiling of SJ and SJH groups using a 3D microtissue
251 organoid model. We co-cultured SW480 with primary rat hepatocytes and 3T3-J2 fibroblasts
252 within collagen I-based microtissues (**Figure 6A**). Conditions included SJ cells and SJH using
253 the same cell numbers and proportions as 2D co-culture. The SJH tricultures alongside co-
254 culture controls were maintained for 7 days before harvesting for transcriptional and
255 metabolic analyses. To identify transcriptional alterations that occur in cancer cells upon
256 exposure to hepatocytes, we performed bead isolation using antibodies against CD326
257 (EpCAM) to isolate the SW480 tumor cells grown in the presence and absence of
258 hepatocytes and supporting J2s and performed bulk RNA-seq analysis to identify genes and
259 pathways that are modulated when exposed to hepatocytes. We found that exposure of
260 tumor cells to hepatocytes led to increased expression of 708 genes and decreased
261 expression of 762 genes in SW480 cells (adj. $p < 0.05$) (**Figure 6B**). Further analysis of gene
262 ontology (GO) and gene set enrichment analysis (GSEA) demonstrated significant
263 alterations in hallmark pathways of Myc targets and pathways associated with several

264 metabolic processes, including oxidative phosphorylation, metabolism of amino acids, GSH
265 metabolism, and fatty acid metabolism (**Figure 6C-E; Supplemental Table 1,2**). We also
266 compared RNAseq findings to oncogenic pathways (**Figure 6F**). These findings demonstrate
267 that hepatocytes drive transcriptional changes in tumor cells, many of which are associated
268 with changes in metabolic pathways.

269 **Multiomics analysis of differentially expressed genes and static metabolite pools.** Our
270 2D co-culture metabolomics pipeline and 3D transcriptional profiling both identified
271 adaptations in amino acid, biosynthetic, and oxidative pathways. Therefore, we integrated
272 these datasets in 2D to identify metabolite-gene relationships important to the SW480-
273 hepatocyte microenvironment. Multiomic integration of a tumor cell transcription profile
274 and metabolomic datasets can help establish the relationship between bulk metabolic
275 adaptation and tumor cell phenotype. After bead isolation from hepatocytes and 3T3-J2s
276 using antibodies against CD326 (EpCAM), RNA from SW480s was isolated and sequenced.
277 Differentially expressed genes (adj. $p < 0.01$) were combined with significantly altered
278 metabolite pools (**Figure 3B**) for univariate association analysis, recovering 627 mRNAs that
279 were significantly correlated with 255 putative metabolites ($p < 0.001$, **Supplemental Table**
280 **3**). We further filtered this correlation matrix to only include very strong associations ($R >$
281 $|0.98|$) to identify a subset of genes related to metabolic adaptation. A total of 151 unique
282 genes correlated strongly with lactate, orotic acid, glutamyl-glycine (glu-gly), malate, and
283 UMP (**Figure 7A**). In these analyses, positive correlations indicate co-expression in response
284 to co-culture while negative correlations indicate opposing expression pattern in response
285 to co-culture. Given our findings of glutathione metabolism, we chose to look closer at the

286 98 genes that associated with the metabolite glutamyl-glycine for gene-gene relationships
287 (**Figure 7B**). GO enrichment analysis of biological processes of 98 genes associated with glu-
288 gly revealed enrichment regulation of the cell cycle, response to hypoxia, and tissue
289 morphogenesis (**Figure 7C**). Ontologies associated with all 151 genes further included
290 adhesion, hypoxia, and angiogenesis (**Supplemental Figure 6A-B**).

291 In this study we have demonstrated a multiomic platform that uses LC-MS-based
292 untargeted metabolomics approaches and bulk RNA-sequencing to reveal complex
293 interactions in a mixed cell population. Additionally, these approaches can be translated to
294 3D microtissue organoid models. Bioinformatic interrogation of datasets suggests an
295 important adaptation in the oxidative environment and in reactive oxygen species
296 (ROS) homeostasis in the tumor microenvironment upon introduction to hepatocytes.

297

298 **Discussion**

299 This study employed a multiomic approach to uncover metabolic adaptation in the tumor-
300 hepatocyte microenvironment using co-cultures of human colon adenocarcinoma cells
301 (SW480) and primary rat hepatocytes, with the support of murine 3T3-J2 fibroblasts. By
302 integrating untargeted metabolomics, ^{13}C-stable isotope tracing untargeted metabolomics
303 (ITUM), and transcriptomic analysis, we identified several critical metabolic alterations
304 driven by the interaction between tumor cells and hepatocytes. First, co-culture of SW480s
305 with primary hepatocytes significantly altered glucose metabolism. Hepatocytes reduced
306 glucose consumption by 80% and lactate production by 94%, compared to SW480
307 monocultures. This suggests hepatocytes disrupt the classical Warburg effect in SW480

308 cells by influencing glucose metabolism (4, 27, 29). Previous work indicates that aerobic
309 glycolysis is an important adaptation for overcoming hypoxia within the liver, thus
310 suppression by hepatocytes may impact survival (11). Hepatocytes display highly dynamic
311 metabolism that serves to regulate glucose homeostasis. In the presence of high glucose
312 levels, hepatocytes can direct excess glucose molecules to storage as glycogen, *de novo*
313 lipogenesis, or to produce uridine (30). Additionally, hepatocytes can use lactate for
314 gluconeogenesis. Further study is necessary to deconvolute these intersectional and
315 dynamic metabolic programs of varying glucose consumption (by both tumor cells and
316 hepatocytes) and glucose production (hepatocytes) when cells are co-cultured in a manner
317 that mimics the tumor microenvironment.

318 In response to reduced glucose consumption, SW480 cells adapted their fuel utilization.
319 We observed a substantial reduction in ketone bodies and glutamine in the media of co-
320 cultures, indicating increased consumption of these alternative substrates. In absence of
321 glucose, tumor cells can reportedly shift to alternative fuels, such as glutamine, however
322 whether this plasticity extends to ketone bodies is not yet well understood. Ketogenesis has
323 been a topic of interest in cancer research (31). Studies have indicated a relationship
324 between diminished expression of rate-limiting enzyme, 3-hydroxy-3-methylglutaryl
325 synthase 2 (HMGCS2), and tumorigenesis (32-34). Thus, it is also possible diminished
326 ketones in the media is due to reduced production through ketogenesis. Further, targeting
327 ketogenesis has been proposed as a potential therapeutic strategy for inhibiting tumor
328 progression, though responses *in vivo* vary between cancer types and stages (31, 35-38). Our
329 studies suggest an impact of SW480-hepatocyte interaction on ketone body metabolism

330 may represent adaptation for tumor survival. As ketogenic capacity has also been shown to
331 vary across the spectrum of metabolic dysfunction-associated steatotic liver disease
332 (MASLD), further study of the relationship between ketogenesis, cancer, and liver health is
333 warranted.

334 Untargeted metabolomics revealed additional changes in metabolites associated with
335 the TCA cycle and energy metabolism. Notably, acetyl-CoA was elevated, while pyruvate,
336 ATP, and NAD^+ were decreased, highlighting key metabolic nodes affected by hepatocyte
337 presence. The co-culture system revealed a possible metabolic exchange between
338 hepatocytes and SW480 cells, particularly in purine and pyrimidine metabolism. SW480s in
339 co-culture displayed enhanced salvage and reduced uric acid production, coupled with
340 increased pyrimidine biosynthesis. Uric acid can regulate oxidative stress, activity of
341 enzymes related to glucose metabolism, and is associated with development of metabolic
342 syndrome (39). Additionally, uric acid is linked with cancer risk (40, 41). Therefore, the
343 modulation of uric acid levels and purine metabolism may be critical for targeting tumor
344 growth. Further, due to comorbidities of cancer and obesity, the intersection of uric acid and
345 metabolic syndrome in the tumor-hepatocyte niche may be an important area of further
346 study. Recent work has established the pyrimidine intermediate, uridine, as an alternative
347 fuel source for cancer cells in a glucose restricted environment (42, 43). As uridine was
348 elevated in the media of hepatocyte-containing cultures, it is possible SW480s utilize this
349 metabolite to drive activity in the pyrimidine pathway. Further study is needed to understand
350 how access to uridine impacts cancer metabolism in the liver and how flux through these
351 nucleoside pathways may impact the oxidative environment.

352 ^{13}C-stable isotope tracing of mixed cell populations results in convoluted ^{13}C-enrichment
353 datasets that can be difficult to interpret for individual cell populations. For this reason,
354 studies often employ conditioned media exchange to study intercellular metabolic
355 dependencies. These studies are limited by the lack of cellular contact that may be relevant
356 to metabolic interactions and the difficulty adapting these methods toward the more
357 complex and advantageous preclinical models of the microenvironment, such as 3D
358 microtissue organoids. Using unsupervised dimension reduction and association analyses,
359 discriminant ^{13}C-ITUM allows for pathway analysis by identifying 1) enriched isotopologues
360 that discriminate groups and 2) metabolite-metabolite relationships within the
361 discriminating isotopologue set. Therefore, discriminant ^{13}C-ITUM is a form of pathway
362 analysis that highlights co-enriched metabolic pathways characterizing mixed cell
363 populations. This systems-level approach enables specificity to substrate utilization with
364 fewer constraints than metabolic flux analysis.

365 Transcriptomic profiling of SW480s revealed adaptation to metabolic pathways and
366 enrichment of oncogenic pathways, including YAP, PTEN, and MYC. These signaling hubs
367 have been implicated in the regulation of cancer cell metabolism (44-46). Here we observe
368 their regulation in response to the presence of hepatocytes in the tumor microenvironment.
369 Multiomic integration of metabolomics and RNA-seq data further showed that metabolic
370 adaptations were associated with significant transcriptional changes in SW480 cells. These
371 changes were linked to key biological processes, including adhesion, hypoxia response, and
372 angiogenesis, indicating that tumor cells undergo functional adaptation in response to the
373 hepatocyte microenvironment. These results are further supported by co-enrichment

374 networks through a novel analysis of ITUM datasets, which we have called discriminant
375 ITUM. This analysis indicated the importance of glutathione synthesis in differentiating
376 SW480-hepatocyte co-cultures from SW480 controls. Finally, these findings were supported
377 by preliminary studies of a 3D microtissue organoid model, which demonstrated that co-
378 culturing SW480 cells with hepatocytes induces similar transcriptional and metabolic
379 changes observed in 2D co-culture system.

380 While this study provides important insights into the metabolic interplay between tumor
381 cells and hepatocytes, several limitations should be acknowledged. First, the use of 2D co-
382 cultures, though effective in revealing key metabolic interactions, lacks the complexity of *in*
383 *vivo* systems and may not fully capture the spatial and structural dynamics present in the
384 liver microenvironment. Future work in advanced models such as organ-on-a-chip or 3D
385 culture systems could provide more physiologically relevant insights. Additionally, our
386 analysis primarily focused on the metabolic and transcriptional changes in tumor cells,
387 leaving the metabolic impact on hepatocytes underexplored. Future work should involve a
388 comprehensive assessment of hepatocyte responses to tumor interaction, including
389 potential metabolic reprogramming. Mechanistic studies targeting the identified metabolic
390 nodes, such as altered glucose and ketone metabolism or nucleoside exchange, could
391 further elucidate their roles in tumor progression and present potential therapeutic
392 strategies to disrupt these metabolic dependencies.

393

394 **Materials and Methods**

395 *Reagents*

396 LCMS grade water (H2O) (Fisher, W6-4), LCMS grade methanol (MeOH) (Fisher, A456-4),
397 LCMS grade acetonitrile (ACN) (Fisher, A955-4), DMEM (high glucose) (Thermo, 11965092),
398 DMEM (no glucose) (Thermo, A1443001), fetal bovine serum (Biotechne, S11150), Pen/Strep
399 (Thermo, 15140122), L-glutamine (200 mM) (Thermo, 25030081), Phosphate Buffered Saline
400 (PBS) (no CaCl2 or MgCl2) (Thermo, 14190144), Molecular Biology Grade Water (Corning,
401 46-000-CM), Pierce BCA Protein Assay Kit (Thermo, 23225), Genomic DNA kit (blood and
402 cultured cells) (IBI scientific, IB47201). 0.25% Trypsin-EDTA (Corning 25-053-Cl), Hank's
403 Balanced Salt Solution (HBSS) (with CaCl2 or MgCl2) (Gibco 14025-076), Collagenase Type
404 IV (Sigma Aldrich, C5138), Human CD326 (EpCAM) MicroBeads (Miltenyi Biotec, 130-061-
405 101), CD16/CD32 Monoclonal Antibody (Invitrogen 14-0161-82), LS Magnetic Separation
406 Columns (Miltenyi Biotec 130-042-401), QuadroMACS Magnetic Separator (Miltenyi Biotec
407 130-090-976), RNeasy Mini Kit (Qiagen, 74104).

408

409 *2D and 3D culture platform*

410 For both 2D and 3D cultures, 3T3-J2 fibroblasts (Kerafast, Catalog Number: EF3003) and
411 SW480 cells (ATCC, lot Number: 700031955) are maintained in tissue culture flasks until
412 ready for use. Primary rat hepatocytes (PRH, Cryopreserved Male Wistar Rat Plateable
413 Hepatocytes AMY 7 mil, Catalog Number: r3000.H15 Lot No. 1210326) were thawed
414 immediately before use. 3T3-J2 fibroblasts are growth arrested using 1 μg/mL mitomycin-C
415 for 4 hours in culture before detachment using trypsin-EDTA.

416 In 2D, 150k PRH and 150k 3T3-J2 fibroblasts are plated per well for all HJ, SJH, SJ wells.
417 On day 7, 50k SW480 cells are seeded to SJH and SJ wells. On day 9, cell culture media is

418 changed to exchange equimolar (22 mM) unlabeled glucose for non-radioactive, stable
419 isotopically labeled 22 mM [U-$^{13}C_6$]glucose according to previously established protocols
420 (47). Cells and final conditioned media are collected on day 10.

421 3D microtissue organoids were fabricated as previously described (25). Briefly, plates
422 were with 2% agarose and allowed to stiffen for 24 hours. We then used a microwell stamp
423 made from a PDMS mold to create 200 μM microwells that held the microtissues separately
424 within the same well. After cleaning the microwells with a series of washes, we added media
425 to the wells. We maintained the microtissues in Human Hepatocyte Maintenance Media
426 (HHM) (43.25mL 1x DMEM, 5 mL Bovine Serum, 750 μL HEPES, 1M, pH 7.6, 500 μL
427 insulin/human transferring/selenous acid and linoleic acid premix (Corning premix
428 solution), 500 μL Penicillin-streptomycin, 100X solution of 50 mg/mL stock, 0.5 μL
429 Dexamethasone, 10 mM in DMSO, 0.5 μL Glucagon, 0.7 mg/mL in 0.05 M acetic acid. During
430 the study, we provided fresh media changes every 48 hours by removing 300 μL from each
431 well and replacing it with 300 μL of fresh media. We then removed the microtissues at their
432 respective time point.

433 *Quantification of Glucose and Lactate via 1 H NMR*

434 ~50 μL of cell culture media was dried to completion in a SpeedVac in the presence of D_2O
435 to aid in water suppression. Samples were reconstituted in D_2O (99.9%) spiked with 0.3 mM
436 d_4-trimethyl-silyl propionate (TSP). ^{1}H-NMR signals were acquired using a Bruker Avance III
437 600 NMR instrument equipped with a CryoProbe, then the integrated intensities of the α-
438 anomeric proton on glucose carbon-1, the methyl signal for lactate, and the tri-methyl signal

439 from TSP, were used to calculate molar concentrations of the respective substrates. For all
440 ^{1}H-NMR collections, spectra were collected by conventional pulse-and-collect
441 measurements under quantitative conditions (10-ppm spectral range using ~15 μs [90°]
442 excitation pulse and 22-second delay between each of 20 transients).

443 *Untargeted Metabolomics and Isotope Tracing Untargeted Metabolomics pipeline*

444 Cells are harvested, metabolites extracted, and raw data acquired using liquid
445 chromatography (LC) on a Thermo Vanquish UHPLC system, and full-scan high-resolution
446 mass spectrometry (HR-MS) on a Thermo QExactive plus hybrid quadrupole-orbitrap mass
447 spectrometer fitted with heated electrospray ionization source and operated in negative and
448 positive polarity mode.

449 **Cell collection for metabolomics.** Media was collected and snap frozen, then adherent
450 cells were washed twice with 1 mL warm (37°C) PBS (-MgCl2, -CaCl2), once with warm
451 (37°C) cell-culture grade H2O, then the entire plate was submerged into liquid nitrogen to
452 snap freeze cells, which rapidly quenches metabolism. To preserve the metabolome, cells
453 were scraped in 500 μL of cold (-20°C) LCMS grade MeOH per well of cells. Two wells were
454 combined to form each replicate, n = 3 per group. Finally, MeOH was evaporated using a
455 SpeedVac. Dried cell pellets were stored at -80°C until analysis.

456 **Metabolite extraction.** Metabolites from cell pellets and conditioned media were
457 extracted and analyzed by LC-MS untargeted metabolomics according to previously
458 published protocols (47, 48). Briefly, cell pellets are reconstituted in 1 mL 2:2:1 (v/v/v)
459 ACN:MeOH:Water, then vortexed (30s), flash frozen in liquid nitrogen (1 min), and sonicated
460 (25°C, 10 min) in three cycles. After 1 hour at -20°C, samples are centrifuged at 15k x g at 4°C

461 for 10 minutes. Supernatant was transferred to a fresh tube and dried by SpeedVac
462 overnight, while the remaining cell pellet was stored at -80°C after removing any remaining
463 solvent for DNA quantification. Cell extracts are reconstituted in 40 µL 1:1 (v/v) ACN:Water
464 for analysis. 20 µL of conditioned media was extracted in 80 µL 1:1 (v/v) ACN:MeOH. Media
465 underwent a single cycle of vortex and sonication, then followed the same procedure as cell
466 pellets. Media samples were reconstituted in 200 µL 1:1 (v/v) ACN:Water for analysis.

467 **Data acquisition.** For this study, polar metabolites were acquired using hydrophilic
468 interaction chromatography (HILIC) and energy nucleotides were acquired by reverse phase
469 (RP), using two unique UHPLC methods: **[1]** SeQuant ZIC-pHILIC column (2.1 x 150 mm, 5
470 µm) (Millipore Sigma, 1.50460). Mobile phase A (MPA) was 95% H2O, 5% ACN, 10 mM
471 ammonium acetate, and 10 mM ammonium hydroxide. Mobile phase B (MPB) was 100%
472 ACN. The total run time was 50 minutes, flow rate was 2 mL/min, column chamber was set
473 to 45°C, and 2 µL sample was injected. Mobile phase gradient was as follows: 0-0.5 min,
474 90% MPB; 0.5-30 min, 90→30% MPB; 30-31 min, 30% MPB; 31-32 min, 30→0% MPB; 32-33
475 min, 0→90% MPB; 33-50 min, 90% MPB. **[2]** Energy nucleotides (ATP, ADP and AMP), and
476 redox nucleotides (NAD^+ and NADH) were measured as previously described, with
477 modifications. Briefly, metabolites were extracted from cells for ITUM in MeOH:ACN:H2O
478 (2:2:1), then extracts were separated and detected using ion-pairing RP UHPLC-MS/MS on a
479 C18 column (Waters Xbridge, 150 x 2.1mm, 3µm). Nucleotides were detected as adducts of
480 dibutylamine acetate on a Thermo QExactive Plus mass spectrometer, operated in positive
481 ionization mode, using parallel reaction monitoring transitions as previously described.

482 For all metabolomics pipelines, both blanks and pooled quality control (QC) samples are
483 injected periodically throughout the run. Blanks were ACN:H2O (1:1) and the QC sample was
484 a pooled sample including all naturally-occurring and ^{13}C-labeled samples. To aid in
485 chemical feature identification, two additional samples were also injected. First, was a
486 standard mix consisting of authentic standards, for all expected analytes. Second, was a
487 pooled sample consisting only of the naturally-occurring samples, analyzed via data-
488 dependent analysis (DDA) tandem mass spectrometry (MS/MS) using IE omics script and R-
489 Studio (49).

490 **Data preparation.** Data processing and initial analysis was performed using Thermo
491 Compound Discoverer 3.3. After raw mass spectra were uploaded, background ions were
492 removed, retention time (RT) for detected signals were aligned across samples, chemical
493 formulas were predicted, then grouped chemical features were profiled to determine
494 compound identity, based on (1) the m/z predicted from the chemical formula, (2) the RT
495 compared to an authentic external standard, and (3) the MS/MS fragmentation pattern,
496 compared to in-house standards or online databases.

497 For ITUM experiments, putatively identified metabolites and lipids were then carried
498 forward and [^{13}C] stable-isotope enrichment with correction for natural abundance. To carry
499 out [^{13}C] stable isotope tracing, all [^{13}C] mass isotopomers (*i.e.,* isotopologues) within the
500 isotopic envelope of each identified metabolic pool were identified based on the diagnostic
501 shift in m/z (Δm/z = 1.0033 Da, natural abundance, 1.11% of all carbon) induced by the
502 presence of ^{13}C-labeled compounds. Raw ion counts for each isotopologue were extracted,
503 summed, and expressed as a percentage of the total pool. After natural abundance

504 correction, the fractional intensities were then graphed as a function of [^{13}C] content,
505 generating mass isotopologue distributions (MIDs) for each detected metabolite or lipid.
506 For static pool analysis, total ion counts were exported from Compound Discoverer and
507 normalized to biomass (either total DNA or total protein). DNA was quantified from cell
508 pellets after metabolite extraction using IBI Scientific genomic DNA kit for cultured cells as
509 previously described for metabolite normalization following kit instructions (50). Total
510 protein was quantified using the Pierce BCA Protein Assay Kit from separately cultured and
511 harvested samples in parallel with metabolomics experiments.

512 *Quantification of Total Ketone Bodies*

513 Acetoacetate (AcAc) and β-hydroxybutyrate (BOHB) were formally quantified using UHPLC-
514 MS/MS as described previously (51, 52). Briefly, [U-$^{13}C_4$]AcAc and [3,4,4,4-D4]βOHB internal
515 standards were spiked into ice cold MeOH:ACN (1:1), then ketones were extracted,
516 separated via reverse-phase UHPLC, and detected via parallel reaction monitoring (PRM) on
517 a QExactive Plus hybrid quadrupole-orbitrap mass spectrometer.

518 *Bulk RNA sequencing and analysis*

519 For the 2D platform, cells were collected from the plates using 0.25% Trypsin-EDTA. For the
520 3D platform, microtissues were collected from the wells and dissociated by incubating at
521 37°C with 0.1mg/mL Collagenase Type IV in HBSS (+CaCl2, +MgCl2) for 30 minutes, then
522 manually disrupted to form a single cell suspension. For both platforms, 8 wells were
523 combined to form replicates, n=3 per group. The single cell suspensions were incubated with
524 MicroBeads against human CD326 (EpCAM) and antibody against CD16/CD32 to block

525 nonspecific binding, then isolated across Miltenyi LS magnetic separation columns. RNA
526 was isolated from the sorted SW480 cells using a Qiagen RNeasy Mini Kit.

527 **Bulk RNA-seq Analysis**. RNA-seq analysis was performed at the Minnesota
528 Supercomputing Institute at the University of Minnesota. Briefly, Fastq files were first
529 processed with the CHURP pipeline (version 0.2.3) (53) to perform adaptor trimming using
530 trimmomatic (version 0.33) (54); reads were then mapped to Homo sapiens GRCh38
531 genome using HiSat2 (version 2.1.0) (55). Subreads count was generated using the Subreads
532 featureCounts tool (version 1.6.2) (56) using the Homo_sapiens.GRCh38.100.gtf annotation.
533 Count data were filtered by removing genes that were less than 300 nt in length and including
534 only genes that had a cpm (counts per million) value greater than 1 cpm in at least two
535 sample replicates. The quasi-likelihood test was used to evaluate differential expression
536 (DE) with edgeR (version 3.38.1) (57, 58). The Benjamini-Hochberg method was used to
537 adjust p-values for multiple hypothesis testing and an adjusted p-value ≤ 0.05, with a log2
538 fold change > 0 was used as a DE significance threshold. For gene ontology (GO pathway and
539 GSEA analysis, the R package clusterProfiler (version 4.4.4) (59, 60) was used. Normalized
540 Enrichment Score (NES) indicates the distribution of genes across a ranked list and
541 normalizes the correlation between gene sets and datasets to gene set size, allowing for
542 comparison. For GSEA analysis specifically, Hallmark and 18 selected C2 pathways were
543 combined and used for testing (see full GSEA pathway results and selected C2 pathways in
544 **Supplemental Table 1, 2**). Analysis of GSEA C6 oncogenic pathways, read counts were
545 converted to normalized counts using the DESeq2 (version 1.42.0) R package and were
546 further filtered to get rid of genes with zero expression across all samples. GSEA was then

547 performed using the standalone software (version 4.3.2) developed by the Broad Institute,
548 and statistical significance was assessed via gene set permutation testing (1000
549 permutations) (61, 62). GEO accession number GSE282081.

550 *Statistics and Multi-omic Analysis*

551 Descriptive data are expressed as mean and standard error (SEM) for continuous measures.
552 Comparison of metabolite abundance were made between HJ and SJH or SJ and SJH by
553 unpaired t-test and corrected for multiple comparisons by Benjamini-Hochberg using
554 GraphPrism v10.2.3. Multi-omic integration of bulk transcriptomic and metabolomics
555 datasets were performed in R v4.2.3 using rcorr() from the Hmisc package and the igraph
556 package for visualization of correlations. Given the small dataset, only highly significant
557 correlations (p-value of Pearson correlation coefficient < 0.001) were included in
558 downstream pathway and gene ontology analysis. Genes that correlated strongly with
559 metabolites of interest were included as a set of gene IDs and fold changes in an
560 ExpressAnalyst query for functional analysis (63).

561 Discriminant ITUM was performed using a curated dataset of positively identified
562 metabolites by commercial standard and / or MS/MS match in mzCloud. Selected
563 metabolites showed significant total enrichment in the SJH group after correction for natural
564 abundance of ^{13}C (1.11% of all carbon in nature), performed within the Compound
565 Discoverer "stable isotope labeling" node based on predicted chemical formula. All
566 isotopologues with enrichment were included for a given metabolite as individual variables,
567 *i.e.* S_M0, S_M1, S_M2, S_M3 included as four unique variables representing serine
568 enrichment. Data presented in 0-100 range and represents percentage of the total

metabolite pool detected by LC-MS in full scan (MS1). Total pools are calculated by sum of ion counts for each possible isotopologue (*i.e.* total ion counts of serine = S_M0 + S_M1 + S_M2 + S_M3; % Enrichment of S_M3 = ion counts of S_M3 / total ion counts of serine * 100). The resulting multivariate dataset was used for Principal Components Analysis (PCA) to identify co-enriched isotopologues that discriminate SJH co-cultures from SJ or HJ controls. PCA was performed in GraphPrism v10.2.3. Data was standardized prior to PCA. A correlation network was graphed from the top contributing isotopologues distinguishing SJH from SJ controls using the igraph package in the R environment for qualitative pathway analysis of glucose utilization in mixed cell populations. Joint pathway analysis of 3D microtissue transcriptomics and metabolomics datasets performed in MetaboAnalyst 4.0 (64).

Acknowledgements: We are grateful to Alisha Seay for technical support. This study was funded by the University of Minnesota, Medical School Dean's Academic Investment Research Program (AIRP). Additional funding: R01DK091538 (PAC); T32DK007203 (ABN); R01CA215052 (KLS); HL166142 (EDQ).

References

1. Siegel RL, Giaquinto AN, and Jemal A. Cancer statistics, 2024. *CA: A Cancer Journal for Clinicians*. 2024;74(1):12-49.
2. Horn SR, Stoltzfus KC, Lehrer EJ, Dawson LA, Tchelebi L, Gusani NJ, et al. Epidemiology of liver metastases. *Cancer Epidemiology*. 2020;67:101760.
3. Hanahan D, and Weinberg Robert A. Hallmarks of Cancer: The Next Generation. *Cell*. 2011;144(5):646-74.
4. Pavlova Natalya N, and Thompson Craig B. The Emerging Hallmarks of Cancer Metabolism. *Cell Metabolism*. 2016;23(1):27-47.
5. Lyssiotis CA, and Kimmelman AC. Metabolic Interactions in the Tumor Microenvironment. *Trends in Cell Biology*. 2017;27(11):863-75.
6. Sullivan MR, Danai LV, Lewis CA, Chan SH, Gui DY, Kunchok T, et al. Quantification of microenvironmental metabolites in murine cancers reveals determinants of tumor nutrient availability. *eLife*. 2019;8:e44235.
7. Lin J, Rao D, Zhang M, and Gao Q. Metabolic reprogramming in the tumor microenvironment of liver cancer. *Journal of Hematology & Oncology*. 2024;17(1):6.
8. Fowle-Grider R, Rowles JL, Shen I, Wang Y, Schwaiger-Haber M, Dunham AJ, et al. Dietary fructose enhances tumour growth indirectly via interorgan lipid transfer. *Nature*. 2024.
9. Huang Q, Tan Y, Yin P, Ye G, Gao P, Lu X, et al. Metabolic Characterization of Hepatocellular Carcinoma Using Nontargeted Tissue Metabolomics. *Cancer Research*. 2013;73(16):4992-5002.
10. Nwosu ZC, Megger DA, Hammad S, Sitek B, Roessler S, Ebert MP, et al. Identification of the Consistently Altered Metabolic Targets in Human Hepatocellular Carcinoma. *Cellular and Molecular Gastroenterology and Hepatology*. 2017;4(2):303-23.e1.
11. Dupuy F, Tabariès S, Andrzejewski S, Dong Z, Blagih J, Annis Matthew G, et al. PDK1-Dependent Metabolic Reprogramming Dictates Metastatic Potential in Breast Cancer. *Cell Metabolism*. 2015;22(4):577-89.
12. Bu P, Chen K-Y, Xiang K, Johnson C, Crown SB, Rakhilin N, et al. Aldolase B-Mediated Fructose Metabolism Drives Metabolic Reprogramming of Colon Cancer Liver Metastasis. *Cell Metabolism*. 2018;27(6):1249-62.e4.
13. Loo Jia M, Scherl A, Nguyen A, Man Fung Y, Weinberg E, Zeng Z, et al. Extracellular Metabolic Energetics Can Promote Cancer Progression. *Cell*. 2015;160(3):393-406.
14. Clish CB. Metabolomics: an emerging but powerful tool for precision medicine. *Cold Spring Harb Mol Case Stud*. 2015;1(1):a000588.
15. Patti GJ, Yanes O, and Siuzdak G. Innovation: Metabolomics: the apogee of the omics trilogy. *Nat Rev Mol Cell Biol*. 2012;13(4):263-9.
16. Nelson AB, Chow LS, Stagg DB, Gillingham JR, Evans MD, Pan M, et al. Acute aerobic exercise reveals FAHFAs distinguish the metabolomes of overweight and normal weight runners. *JCI Insight*. 2022.
17. Jang C, Chen L, and Rabinowitz JD. Metabolomics and Isotope Tracing. *Cell*. 2018;173(4):822-37.

18. Puchalska P, Martin SE, Huang X, Lengfeld JE, Daniel B, Graham MJ, et al. Hepatocyte-Macrophage Acetoacetate Shuttle Protects against Tissue Fibrosis. *Cell Metab*. 2019;29(2):383-98 e7.
19. Stagg DB, Gillingham JR, Nelson AB, Lengfeld JE, d'Avignon DA, Puchalska P, et al. Diminished ketone interconversion, hepatic TCA cycle flux, and glucose production in D-β-hydroxybutyrate dehydrogenase hepatocyte-deficient mice. *Molecular Metabolism*. 2021;53:101269.
20. Puchalska P, Huang X, Martin SE, Han X, Patti GJ, and Crawford PA. Isotope Tracing Untargeted Metabolomics Reveals Macrophage Polarization-State-Specific Metabolic Coordination across Intracellular Compartments. *iScience*. 2018;9:298-313.
21. Buescher JM, Antoniewicz MR, Boros LG, Burgess SC, Brunengraber H, Clish CB, et al. A roadmap for interpreting 13C metabolite labeling patterns from cells. *Current Opinion in Biotechnology*. 2015;34:189-201.
22. Muir A, Danai LV, and Vander Heiden MG. Microenvironmental regulation of cancer cell metabolism: implications for experimental design and translational studies. *Disease Models & Mechanisms*. 2018;11(8):dmm035758.
23. Xiang C, Du Y, Meng G, Soon Yi L, Sun S, Song N, et al. Long-term functional maintenance of primary human hepatocytes in vitro. *Science*. 2019;364(6438):399-402.
24. Sun P, Zhang G, Su X, Jin C, Yu B, Yu X, et al. *Cell Reports*. 2019;29(10):3212-22.e4.
25. Kukla DA, Crampton AL, Wood DK, and Khetani SR. Microscale Collagen and Fibroblast Interactions Enhance Primary Human Hepatocyte Functions in Three-Dimensional Models. *Gene expression*. 2020;20(1):1-18.
26. DeBerardinis RJ, and Chandel NS. We need to talk about the Warburg effect. *Nature Metabolism*. 2020;2(2):127-9.
27. Warburg O. The metabolism of carcinoma cells. *The Journal of Cancer Research*. 1925;9(1):148-63.
28. Ma EH, Verway MJ, Johnson RM, Roy DG, Steadman M, Hayes S, et al. Metabolic Profiling Using Stable Isotope Tracing Reveals Distinct Patterns of Glucose Utilization by Physiologically Activated CD8⁺ T Cells. *Immunity*. 2019;51(5):856-70.e5.
29. Liberti MV, and Locasale JW. The Warburg Effect: How Does it Benefit Cancer Cells? *Trends Biochem Sci*. 2016;41(3):211-8.
30. Deng Y, Wang ZV, Gordillo R, An Y, Zhang C, Liang Q, et al. An adipo-biliary-uridine axis that regulates energy homeostasis. *Science*. 2017;355(6330).
31. Puchalska P, and Crawford PA. In: Stover PJ, and Balling R eds. *Annual Review of Nutrition, Vol 41, 2021*. 2021:49-77.
32. Camarero N, Mascaró C, Mayordomo C, Vilardell F, Haro D, and Marrero PF. Ketogenic HMGCS2 Is a c-Myc target gene expressed in differentiated cells of human colonic epithelium and down-regulated in colon cancer. *Mol Cancer Res*. 2006;4(9):645-53.
33. Wang YH, Liu CL, Chiu WC, Twu YC, and Liao YJ. HMGCS2 Mediates Ketone Production and Regulates the Proliferation and Metastasis of Hepatocellular Carcinoma. *Cancers (Basel)*. 2019;11(12).

672 34. Zou K, Hu Y, Li M, Wang H, Zhang Y, Huang L, et al. Potential Role of HMGCS2 in Tumor
673 Angiogenesis in Colorectal Cancer and Its Potential Use as a Diagnostic Marker. *Can*
674 *J Gastroenterol Hepatol*. 2019;2019:8348967.
675 35. Zhang J, Jia PP, Liu QL, Cong MH, Gao Y, Shi HP, et al. Low ketolytic enzyme levels in
676 tumors predict ketogenic diet responses in cancer cell lines in vitro and in vivo. *J Lipid*
677 *Res*. 2018;59(4):625-34.
678 36. Shukla SK, Gebregiworgis T, Purohit V, Chaika NV, Gunda V, Radhakrishnan P, et al.
679 Metabolic reprogramming induced by ketone bodies diminishes pancreatic cancer
680 cachexia. *Cancer Metab*. 2014;2:18.
681 37. Sperry J, Condro MC, Guo L, Braas D, Vanderveer-Harris N, Kim KKO, et al.
682 Glioblastoma Utilizes Fatty Acids and Ketone Bodies for Growth Allowing Progression
683 during Ketogenic Diet Therapy. *iScience*. 2020;23(9):101453.
684 38. Xia S, Lin R, Jin L, Zhao L, Kang HB, Pan Y, et al. Prevention of Dietary-Fat-Fueled
685 Ketogenesis Attenuates BRAF V600E Tumor Growth. *Cell Metab*. 2017;25(2):358-73.
686 39. Lima WG, Martins-Santos ME, and Chaves VE. Uric acid as a modulator of glucose
687 and lipid metabolism. *Biochimie*. 2015;116:17-23.
688 40. Yiu A, Van Hemelrijck M, Garmo H, Holmberg L, Malmström H, Lambe M, et al.
689 Circulating uric acid levels and subsequent development of cancer in 493,281
690 individuals: findings from the AMORIS Study. *Oncotarget*. 2017;8(26):42332-42.
691 41. Fini MA, Elias A, Johnson RJ, and Wright RM. Contribution of uric acid to cancer risk,
692 recurrence, and mortality. *Clin Transl Med*. 2012;1(1):16.
693 42. Nwosu ZC, Ward MH, Sajjakulnukit P, Poudel P, Ragulan C, Kasperek S, et al. Uridine-
694 derived ribose fuels glucose-restricted pancreatic cancer. *Nature*.
695 2023;618(7963):151-8.
696 43. Skinner OS, Blanco-Fernández J, Goodman RP, Kawakami A, Shen H, Kemény LV, et
697 al. Salvage of ribose from uridine or RNA supports glycolysis in nutrient-limited
698 conditions. *Nature Metabolism*. 2023;5(5):765-76.
699 44. Dong Y, Tu R, Liu H, and Qing G. Regulation of cancer cell metabolism: oncogenic
700 MYC in the driver's seat. *Signal Transduction and Targeted Therapy*. 2020;5(1):124.
701 45. Chen C-Y, Chen J, He L, and Stiles BL. PTEN: Tumor Suppressor and Metabolic
702 Regulator. *Frontiers in Endocrinology*. 2018;9.
703 46. Zhang X, Zhao H, Li Y, Xia D, Yang L, Ma Y, et al. The role of YAP/TAZ activity in cancer
704 metabolic reprogramming. *Molecular Cancer*. 2018;17(1):134.
705 47. Puchalska P, and Crawford PA. Application of Stable Isotope Labels for Metabolomics
706 in Studies in Fatty Liver Disease. *Methods Mol Biol*. 2019;1996:259-72.
707 48. Ivanisevic J, Zhu Z-J, Plate L, Tautenhahn R, Chen S, O'Brien PJ, et al. Toward 'Omic
708 Scale Metabolite Profiling: A Dual Separation–Mass Spectrometry Approach for
709 Coverage of Lipid and Central Carbon Metabolism. *Analytical Chemistry*.
710 2013;85(14):6876-84.
711 49. Koelmel JP, Kroeger NM, Gill EL, Ulmer CZ, Bowden JA, Patterson RE, et al. Expanding
712 Lipidome Coverage Using LC-MS/MS Data-Dependent Acquisition with Automated
713 Exclusion List Generation. *Journal of the American Society for Mass Spectrometry*.
714 2017;28(5):908-17.

50. Silva LP, Lorenzi PL, Purwaha P, Yong V, Hawke DH, and Weinstein JN. Measurement of DNA Concentration as a Normalization Strategy for Metabolomic Data from Adherent Cell Lines. *Analytical Chemistry*. 2013;85(20):9536-42.
51. Puchalska P, Nelson AB, Stagg DB, and Crawford PA. Determination of ketone bodies in biological samples via rapid UPLC-MS/MS. *Talanta*. 2021;225:122048.
52. Queathem ED, Nelson AB, and Puchalska P. In: Giera M, and Sánchez-López E eds. *Clinical Metabolomics: Methods and Protocols*. New York, NY: Springer US; 2025:117-31.
53. Baller J, Kono T, Herman A, and Zhang Y. *Practice and Experience in Advanced Research Computing 2019: Rise of the Machines (learning)*. Chicago, IL, USA: Association for Computing Machinery; 2019:Article 96.
54. Bolger AM, Lohse M, and Usadel B. Trimmomatic: a flexible trimmer for Illumina sequence data. *Bioinformatics*. 2014;30(15):2114-20.
55. Kim D, Langmead B, and Salzberg SL. HISAT: a fast spliced aligner with low memory requirements. *Nature Methods*. 2015;12(4):357-60.
56. Liao Y, Smyth GK, and Shi W. The Subread aligner: fast, accurate and scalable read mapping by seed-and-vote. *Nucleic Acids Research*. 2013;41(10):e108-e.
57. McCarthy DJ, Chen Y, and Smyth GK. Differential expression analysis of multifactor RNA-Seq experiments with respect to biological variation. *Nucleic Acids Res*. 2012;40(10):4288-97.
58. Robinson MD, McCarthy DJ, and Smyth GK. edgeR: a Bioconductor package for differential expression analysis of digital gene expression data. *Bioinformatics*. 2009;26(1):139-40.
59. The Gene Ontology Consortium. The Gene Ontology Resource: 20 years and still GOing strong. *Nucleic Acids Research*. 2018;47(D1):D330-D8.
60. Yu G, Wang LG, Han Y, and He QY. clusterProfiler: an R package for comparing biological themes among gene clusters. *Omics*. 2012;16(5):284-7.
61. Love MI, Huber W, and Anders S. Moderated estimation of fold change and dispersion for RNA-seq data with DESeq2. *Genome Biology*. 2014;15(12):550.
62. Subramanian A, Tamayo P, Mootha VK, Mukherjee S, Ebert BL, Gillette MA, et al. Gene set enrichment analysis: a knowledge-based approach for interpreting genome-wide expression profiles. *Proc Natl Acad Sci U S A*. 2005;102(43):15545-50.
63. Ewald J, Zhou G, Lu Y, and Xia J. Using ExpressAnalyst for Comprehensive Gene Expression Analysis in Model and Non-Model Organisms. *Current Protocols*. 2023;3(11):e922.
64. Chong J, and Xia J. Using MetaboAnalyst 4.0 for Metabolomics Data Analysis, Interpretation, and Integration with Other Omics Data. *Methods Mol Biol*. 2020;2104:337-60.

755 **Tables**

756 **Table 1.** Differential abundance of select metabolites in SJH co-cultures relative to HJ or SJ
757 controls. FC: fold change; ctrl: control.

Putative metabolite	Log_2 (FC: SJH / ctrl)	Adjusted p-value	Direction; Relative to [HJ] or [SJ]
S-Adenosylhomocysteine	1.87	0.0004	↑; HJ
Pyruvate	-1.05	0.0001	↓; HJ
Acetyl-CoA	-1.98	0.002	↓; HJ
Propionyl-CoA	-1.89	0.012	↓; HJ
Propionyl-CoA	5.01	0.0004	↑; SJ
Glutamyl-glycine	2.47	0.00007	↑; SJ
Acetyl-CoA	1.63	0.016	↑; SJ
Pyruvate	-3.60	0.0006	↓; SJ
Lactate	-2.78	0.0012	↓; SJ
NAD^+	-1.85	0.012	↓; SJ
ATP	-1.09	0.03	↓; SJ

758

759

760 **Table 2.** Differential abundance of select metabolites in SJH co-cultures relative to 1T1
761 dilution. Abbreviations: FC: fold change

Putative metabolite	Log_2 (FC: SJH / HJ)	Adjusted p-value	Direction relative to 1T1
Glutamyl-glycine	2.59	0.0018	↑
Uracil	2.24	0.0044	↑
Uridine diphosphate	1.42	0.021	↑
Aspartate	1.17	0.0018	↑
Malate	1.03	0.0029	↑
Lactate	-1.08	0.013	↓

762

763

764

765 **Table 3.** Fold change in extracellular and intracellular metabolite abundance after 24-hour
766 incubation relative to starting media (t0). Adjusted p-value by t-test comparing T24
767 abundance to T0 abundance with BH correction for multiple testing. Abbreviations: FC: fold
768 change; E: Extracellular; I: Intracellular; NC: no change.

	Log_2 (FC: T24 / T0) [adj. p-value]			
Putative metabolite (E/I)	**HJ**	**SJH**	**SJ**	**Direction relative to T0**
Hypoxanthine (E)	-1.36 [<0.0001]	-2.62 [<0.0001]	-4.73 [<0.00001]	↓; ↓; ↓
Uric Acid (E)	-3.97 [<0.001]	-4.20 [<0.001]	3.17 [<0.001]	↓; ↓; ↑
Inosine (I)	1.00 [0.002]	1.27 [0.003]	-0.42 [0.27]	↑; ↑; NC
Uridine (E)	2.36 [<0.0001]	1.94 [<0.001]	-0.50 [0.15]	↑; ↑; NC
Orotic Acid (E)	4.27 [<0.00001]	4.19 [<0.001]	0.40 [<0.001]	↑; ↑; ↑
Aspartate (I)	0.04 [0.87]	0.55 [0.02]	-0.11 [0.49]	NC; ↑; NC
Carbamoyl aspartate (I)	-0.16 [0.19]	5.47 [0.036]	-0.17 [>0.99]	NC; ↑; NC
UDP (I)	0.32 [0.62]	1.44 [0.017]	0.51 [0.33]	NC; ↑; NC
Uridine (I)	1.13 [0.10]	3.23 [0.005]	-0.25 [0.33]	NC; ↑; NC
Orotic Acid (I)	0.09 [0.62]	3.48 [0.029]	-0.38 [0.37]	NC; ↑; NC

769

770

Figure Legends

Figure 1. Multiomic study of co-cultures of primary hepatocytes and SW480s. (A) Scheme of 2D co-culture system and timeline for cell collection. (B) -Omic coverage of co-cultured groups.

Figure 2. Fuel utilization in 2-dimensional co-cultures. (A) Glucose consumption and lactate production in moles per ng total DNA per day. (B) Lactate / glucose ratio of media concentration after 24h. (C) Concentration of acetoacetate (AcAc), β-hydroxybutyrate (βOHB) and total ketone bodies (TKB) in mmol/g DNA measured in media after 24h incubation. (D) Relative abundance of glutamine in total ion counts after normalization to total ng DNA. Volcano plot showing upregulated and downregulated metabolites in SJH compared to: (E) HJ control cultures and (F) SJ control cultures; positive $\log_2$FC = up in SJH. Significance tested using unpaired t-test, comparison HJ vs SJH or SJ vs SJH, and corrected for multiple comparisons using Benjamini-Hochberg method. *: p adj. < 0.05, **: p adj. < 0.01, ***: p adj. < 0.001, ****: p adj. < 0.0001. Abbreviations: HJ: Hepatocyte+3T3-J2 co-culture; SJH: SW480+3T3-J2+Hepatocyte co-culture; SJ: SW480+3T3-J2 co-culture.

Figure 3. Analytical dilution of co-culture controls reveals metabolic adaptation in SJH co-cultures. (A) Schematic of analytical dilution of HJ and SJ controls to form a 1-to-1 ratio (1T1) after metabolite extraction. (B) Volcano plot upregulated and downregulated metabolites in SJH compared to 1T1 ion counts; positive $\log_2$FC = up in SJH.

Figure 4. Metabolic interactions of biosynthetic pathways in SJH co-cultures. Fold change of metabolite abundance after 24h co-culture relative to time point 0 in: (A) media abundance of purine metabolism products, hypoxanthine and uric acid, (B) intracellular inosine pools, (D) media abundance of pyrimidine biosynthesis intermediates, uridine and orotic acid, and (E) intracellular pyrimidine intermediates and substrates, aspartate, carbamoyl aspartate, orotic acid, UDP, and uridine. (C) ^{13}C-enrichment of intracellular inosine pools from 22 mM [U-$^{13}C_6$]glucose in 3D microtissue organoids. Statistical comparison by unpaired t-test; letters indicate significance in comparison to HJ controls (“a”) or SJ controls (“b”).

Figure 5. Discriminant ITUM analysis of SJH co-cultures. (A) Biplot of first two principal components (PC1, PC2) of PCA of HJ, SJH, and SJ co-cultures by ^{13}C-glucose-enriched

isotopologues. Black filled circles represent samples. Spheres show co-culture groups. Blue directed vectors show isotopologue loadings for PC1 and PC2. (B) Hierarchical clustering of ITUM SJH vs SJ Pearson correlation matrix. White triangle with “1” label indicates control cluster of isotopologues; Yellow shapes with “2” and “3” label corresponds to cluster of isotopologues from region of strongly co-enriched isotopologues in response to co-culture; Black shapes with “4” label corresponds to cluster of isotopologues with weak co-enrichment in response to co-culture. Red arrow, U_M6 positive correlation with unenriched M+0 isotopologues in Region 1; Blue arrow, U_M6 negative correlation with multiple isotopologues including GSH_M3 in Region 2; Yellow arrow, GSH_M4 positive correlation with metabolic precursor E_M4 in Region 3. Abbreviations: M#: isotopologue representing number of heavy carbons present in the molecule (*i.e.,* M1 indicates presence of 1 heavy 13-carbon), aKG: alpha-ketoglutarate, S: serine, M: Malate, L: lactate, C: citrate, ATP: adenosine triphosphate, U: uridine diphosphate N-Acetylglucosamine, G: glycine, D: Asparate, E: Glutamate, GSH: glutathione, Sc: Succinate, GPI: glycerophosphoinositol.

Figure 6. Transcriptional profiling of tumor cells in 3D microtissues identifies alterations in metabolic pathways upon exposure to hepatocytes. (A) 3D microtissue organoid scheme. (B) Volcano plot showing significantly upregulated and downregulated genes in samples from SJH cultures compared with SJ cultures. Positive logFC indicates up in SJH cultures. (C) Gene ontology analysis using DEG as input. (D) GSEA Hallmark analysis of SJ compared with SJH. A positive NES score indicates gene profiles that are enriched in tumor cells from the SJH condition compared with the SJ condition. All shown pathways adjusted FDR < 0.05. (E) Expression patterns of core enriched genes associated with Myc pathway and two metabolic pathways, oxidative phosphorylation and glutathione metabolism, that are positively enriched in the SJH condition and heat maps. (F) GSEA Oncogenic analysis of SJ compared with SJH. A negative NES score indicates gene profiles that are enriched in tumor cells from the SJ condition compared with the SJH condition. All shown pathways adjusted FDR < 0.05.

Figure 7. Multiomic pathway analysis of metabolic adaptation to hepatocytes. (A) Correlation network of differentially expressed genes (DEGs) and metabolites in SJH co-cultures compared to SJ control cultures. Gene names filtered from full bulk RNA-sequencing DEGs for significance of correlation to metabolites of interest ($p < 0.001$). Red lines indicate strong positive associations and blue represent strong negative associations ($R > |0.98|$). (B) Hierarchical clustering of Pearson correlation matrix of transcripts highly correlated with glutamyl-glycine (Glu-Gly). (C) Gene counts with functional group membership of 98 transcripts found to correlate strongly with glutamyl-glycine (Glu-Gly)

841 **Supplemental Figure 1. Metabolite abundance in 2D co-cultures.** Ion counts after
842 normalization to total ng DNA of: (A) pyruvate, (B) Acetyl-CoA, (C) Propionyl-CoA, (D) Lactate,
843 (E) NAD^+, (F) NADH, and (H) AMP, ADP, ATP nucleotides. (G) Ratio of NAD^+ to NADH ion
844 counts. (I) Calculated energy charge of each co-culture group based on ion counts of AMP,
845 ADP, and ATP. Significance tested using unpaired t-test, comparison HJ vs SJH or SJ vs SJH,
846 and corrected for multiple comparisons using Benjamini-Hochberg method. *: p adj. < 0.05,
847 **: p adj. < 0.01, ***: p adj. < 0.001, ****: p adj. < 0.0001.
848
849 **Supplemental Figure 2. Lactate abundance in co-culture and 1T1 dilution.** Bar graph of
850 total ion counts after normalization to DNA compared to analytical dilution (1T1).
851 Significance tested using unpaired t-test, comparison HJ vs SJH or SJ vs SJH, and 1T1 vs SJH;
852 corrected for multiple comparisons using Benjamini-Hochberg method. *: p adj. < 0.05, **:
853 p adj. < 0.01
854
855 **Supplemental Figure 3. Percent change in media purines.** Percent difference in media
856 after 24h incubation with co-cultured cells where time point 0 represents starting media
857 abundance prior to cell exposure. Dotted lines represent accumulation of hypoxanthine
858 (Hpx) and uric acid (UA) after 24h at 37°C in media in absence of cells. Statistical comparison
859 by unpaired t-test; letters indicate significance in comparison to HJ controls ("a") or SJ
860 controls ("b").
861
862 **Supplemental Figure 4. Correlation matrix of SJH vs HJ ITUM in 2D co-cultures.**
863 Correlation matrix assessing co-enriched isotopologues in response to presence of
864 hepatocytes (SJ, SJH cultures). Red gradient represents positive associations while blue
865 represents negative associations. Correlations measuring by Pearson correlation method.
866
867 **Supplemental Figure 5. Distribution of ^{13}C enrichment.** Percent enrichment of total pools
868 of (A) Uridine diphosphate N-acetyglucosamine and (B) glutathione after 24h incubation
869 with [U-$^{13}C_6$]glucose at 37°C. *: p adj. < 0.05
870
871 **Supplemental Figure 6. Multiomic pathway analysis.** (A) Gene counts with functional
872 group membership of 151 genes found to correlate strongly with glutamyl-glycine (Glu-Gly),
873 orotic acid, lactate, uridine monophosphate, and malate. (B) Functional network of shared
874 genes in represented transcriptional profile with strong metabolite-gene associations;
875 analysis performed using ExpressAnalyst. (C) Scatter plot of joint pathway analysis from
876 MetaboAnalyst v4.0 using DEGs and full static metabolomics dataset based on associated
877 fold changes. X and y axes show enrichment score in genes and metabolite peaks,
878 respectively.

A

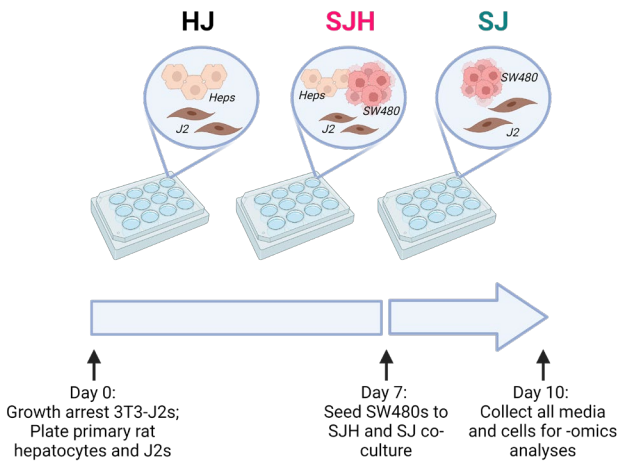
HJ
SJH
SJ
Heps
J2
Heps
SW480
J2
SW480
J2
Day 0:
Growth arrest 3T3-J2s;
Plate primary rat
hepatocytes and J2s
Day 7:
Seed SW480s to
SJH and SJ co-
culture
Day 10:
Collect all media
and cells for -omics
analyses

B

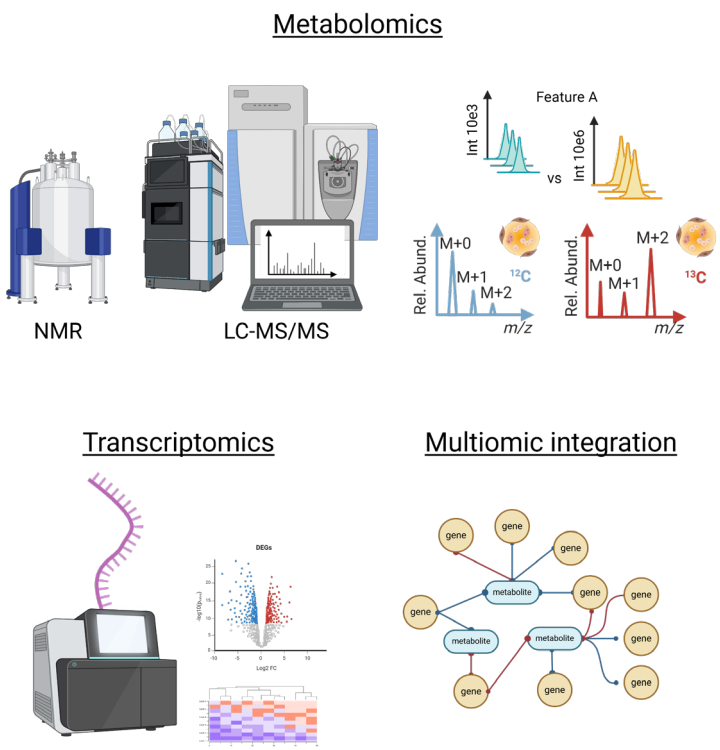
Metabolomics
NMR
LC-MS/MS
Feature A
Int 10e3
vs
Int 10e6
Rel. Abund.
M+0
M+1
M+2
12C
m/z
Rel. Abund.
M+0
M+1
M+2
13C
m/z
Transcriptomics
DEGs
Multiomic integration
gene
metabolite

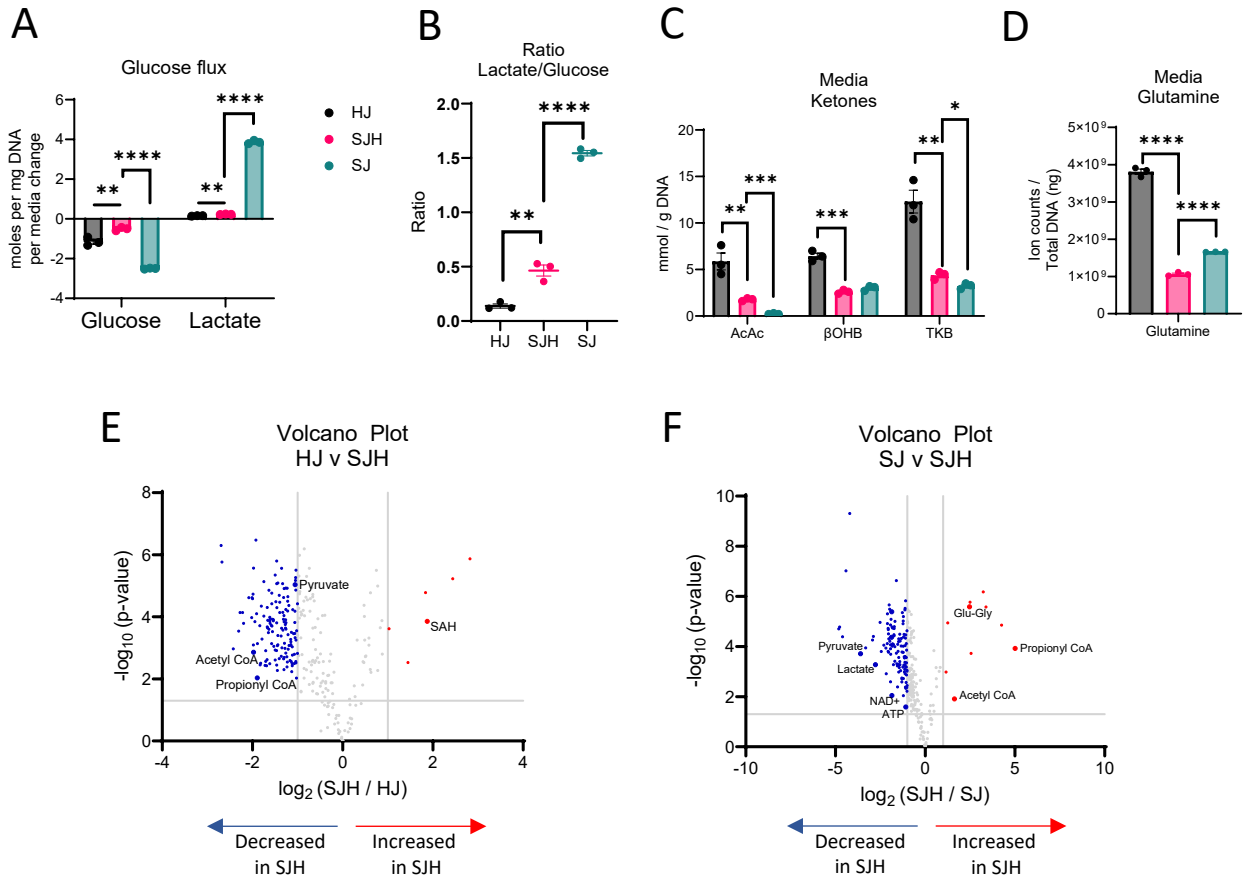
A
Glucose flux
moles per mg DNA per media change
Glucose
Lactate
HJ
SJH
SJ
B
Ratio Lactate/Glucose
Ratio
HJ
SJH
SJ
C
Media Ketones
mmol / g DNA
AcAc
βOHB
TKB
D
Media Glutamine
Ion counts / Total DNA (ng)
Glutamine
E
Volcano Plot HJ v SJH
-log10 (p-value)
log2 (SJH / HJ)
Pyruvate
SAH
Acetyl CoA
Propionyl CoA
Decreased in SJH
Increased in SJH
F
Volcano Plot SJ v SJH
-log10 (p-value)
log2 (SJH / SJ)
Glu-Gly
Propionyl CoA
Pyruvate
Lactate
NAD+
ATP
Acetyl CoA
Decreased in SJH
Increased in SJH

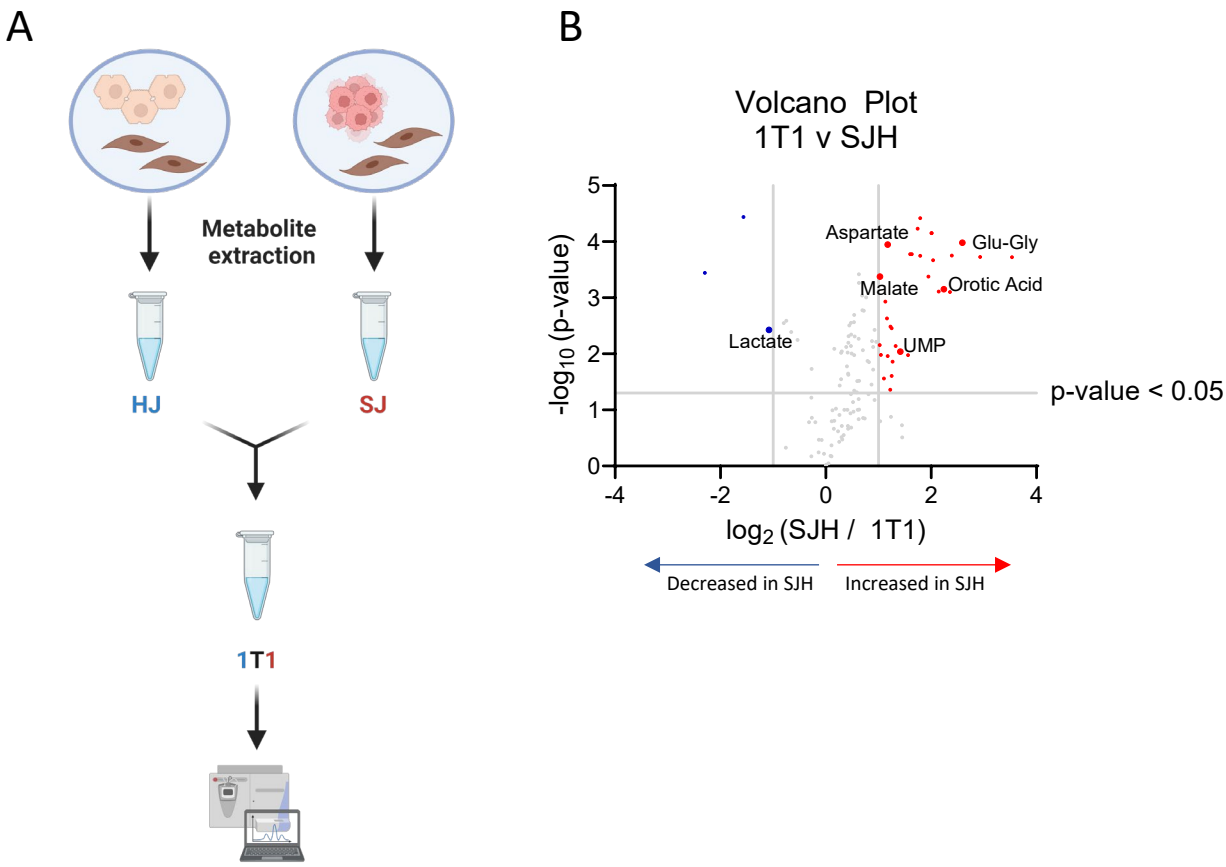
A
Metabolite extraction
HJ
SJ
1T1
B
Volcano Plot
1T1 v SJH
-log10 (p-value)
log2 (SJH / 1T1)
Aspartate
Glu-Gly
Malate
Orotic Acid
Lactate
UMP
p-value < 0.05
Decreased in SJH
Increased in SJH

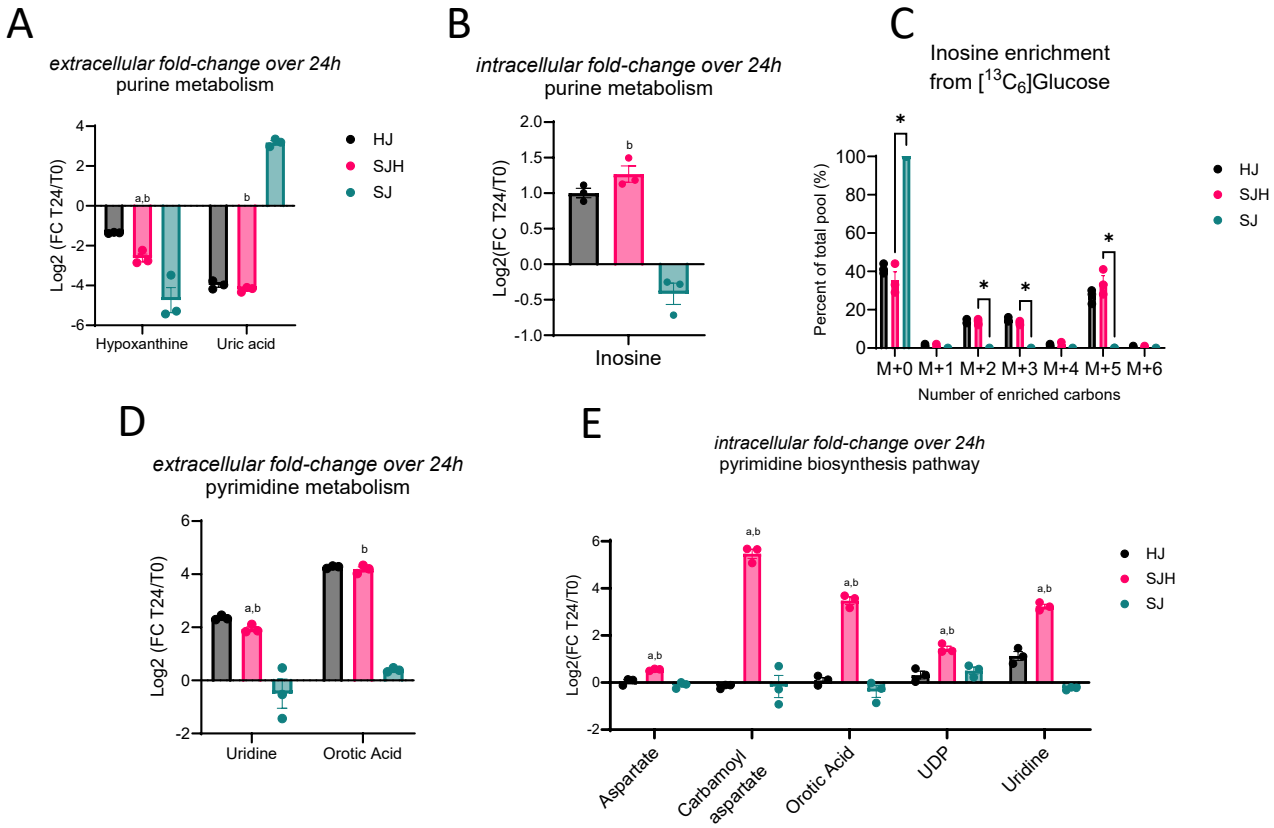
A
extracellular fold-change over 24h
purine metabolism
Log2 (FC T24/T0)
4
2
0
-2
-4
-6
a,b
b
Hypoxanthine
Uric acid
HJ
SJH
SJ
B
intracellular fold-change over 24h
purine metabolism
Log2(FC T24/T0)
2.0
1.5
1.0
0.5
0.0
-0.5
-1.0
b
Inosine
C
Inosine enrichment
from [13C6]Glucose
Percent of total pool (%)
100
80
60
40
20
0
*
*
*
*
M+0
M+1
M+2
M+3
M+4
M+5
M+6
Number of enriched carbons
HJ
SJH
SJ
D
extracellular fold-change over 24h
pyrimidine metabolism
Log2 (FC T24/T0)
6
4
2
0
-2
a,b
b
Uridine
Orotic Acid
E
intracellular fold-change over 24h
pyrimidine biosynthesis pathway
Log2(FC T24/T0)
6
4
2
0
-2
a,b
a,b
a,b
a,b
a,b
Aspartate
Carbamoyl aspartate
Orotic Acid
UDP
Uridine
HJ
SJH
SJ

Figure 5

A

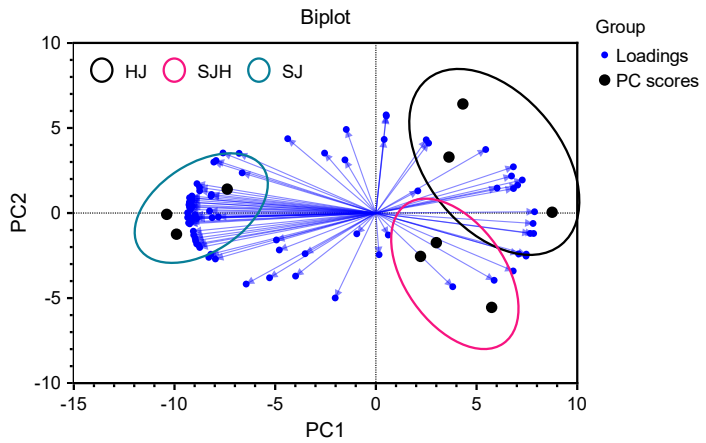
Biplot
Group
Loadings
PC scores
HJ
SJH
SJ
PC2
PC1
10
5
0
-5
-10
-15
-10
-5
0
5
10

B

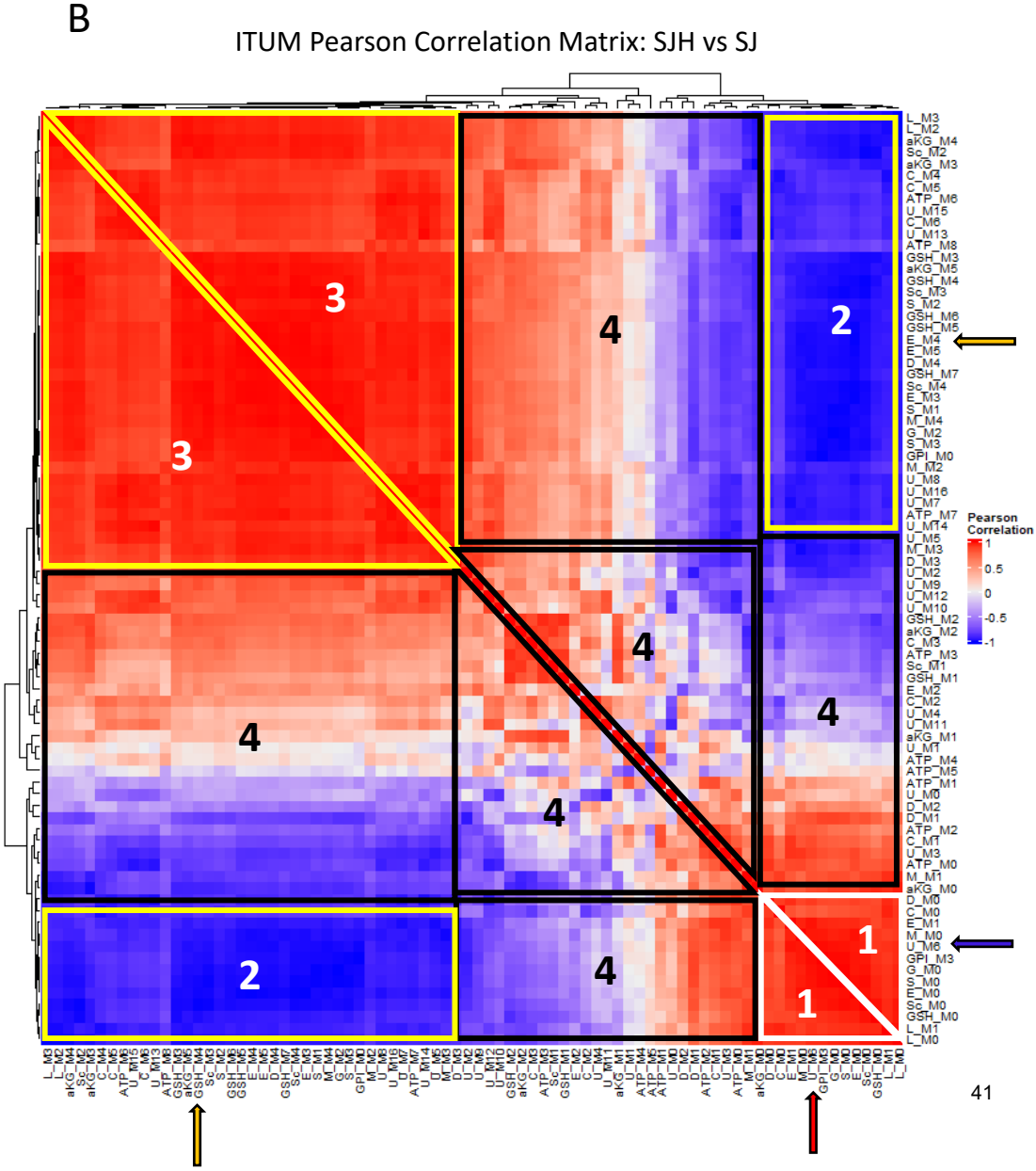
ITUM Pearson Correlation Matrix: SJH vs SJ
Pearson Correlation
1
0.5
0
-0.5
-1
3
3
4
2
4
4
4
4
2
4
1
1

Figure 6

A

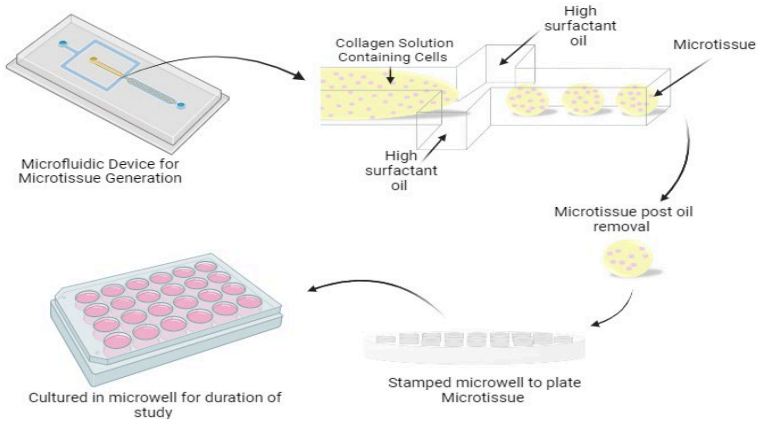

B

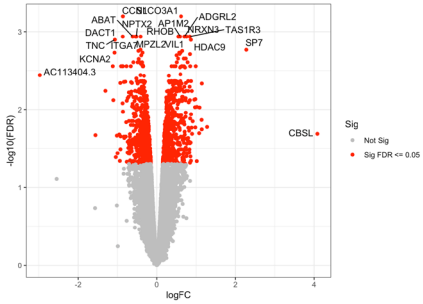

C

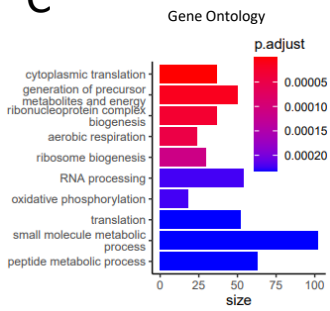

D

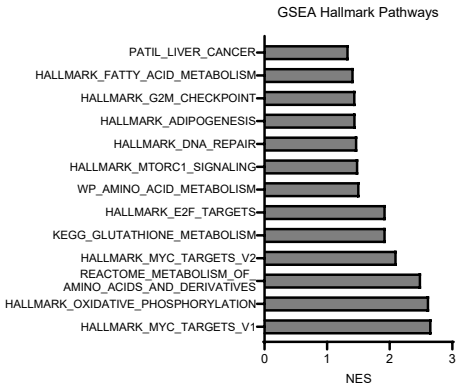

E

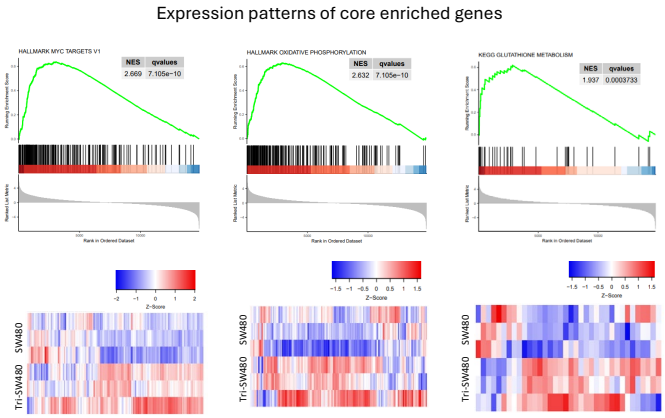

F

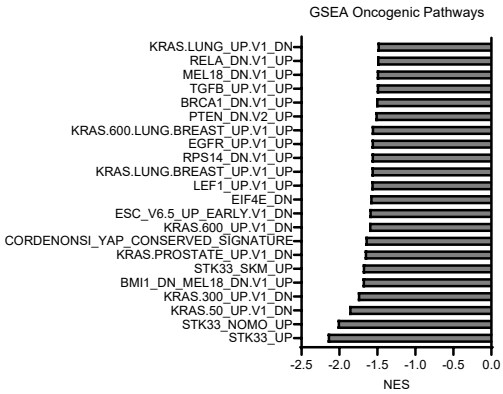

Figure 7

A

Metabolite-Gene Correlation Network

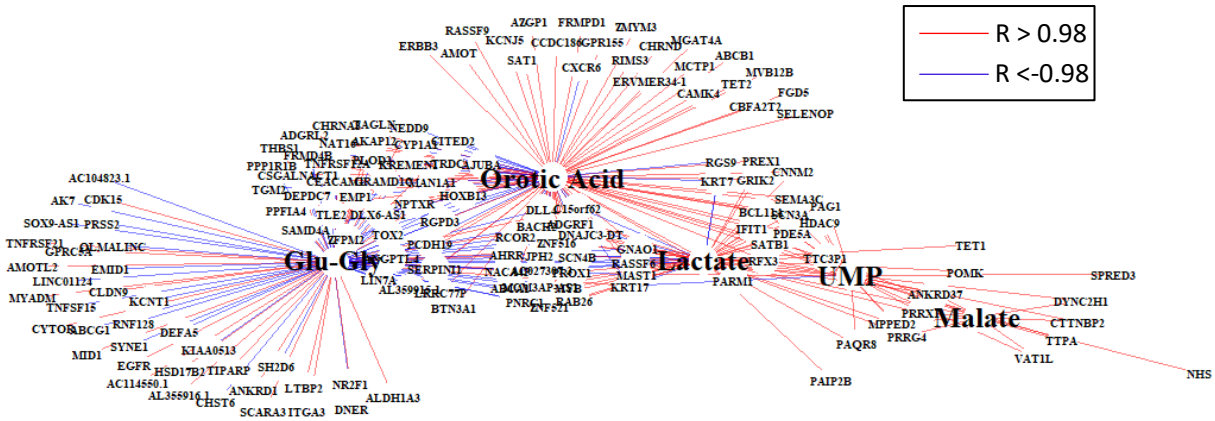

B

Correlation Matrix
Glu-Gly:Transcript Network

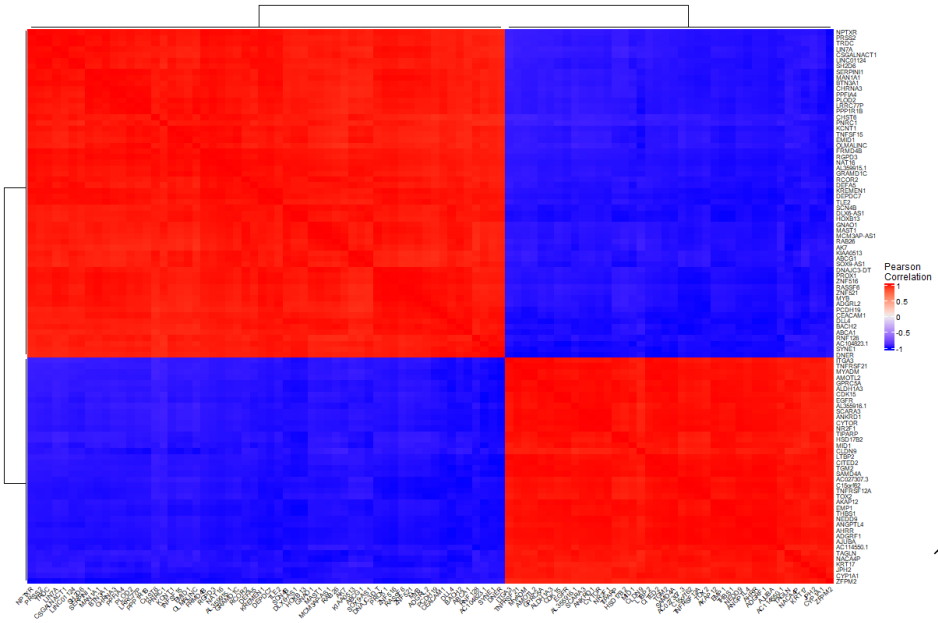

C

GO: Biological Process
Glu-Gly:Transcript Correlation Network

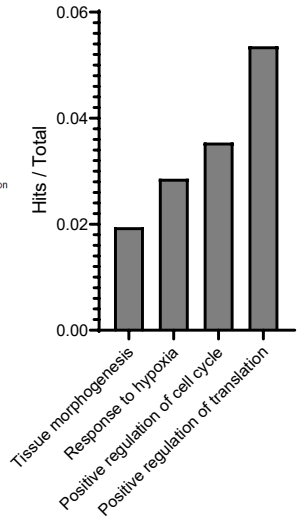

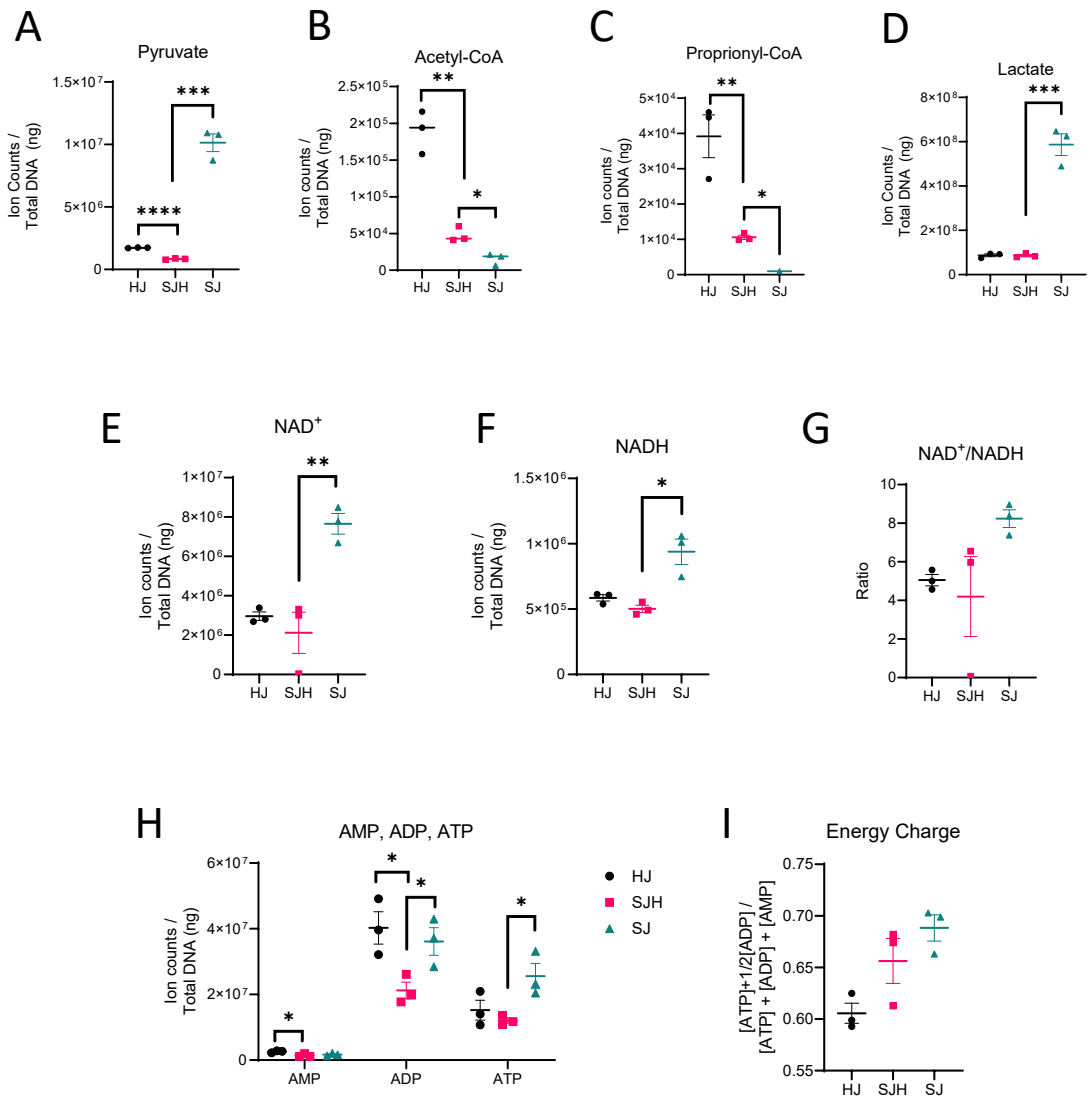
A
Pyruvate
Ion Counts / Total DNA (ng)
1.5×10^7
1×10^7
5×10^6
0
****
***
HJ SJH SJ
B
Acetyl-CoA
Ion counts / Total DNA (ng)
2.5×10^5
2×10^5
1.5×10^5
1×10^5
5×10^4
0
**
*
HJ SJH SJ
C
Proprionyl-CoA
Ion counts / Total DNA (ng)
5×10^4
4×10^4
3×10^4
2×10^4
1×10^4
0
**
*
HJ SJH SJ
D
Lactate
Ion Counts / Total DNA (ng)
8×10^8
6×10^8
4×10^8
2×10^8
0
***
HJ SJH SJ
E
NAD+
Ion counts / Total DNA (ng)
1×10^7
8×10^6
6×10^6
4×10^6
2×10^6
0
**
HJ SJH SJ
F
NADH
Ion counts / Total DNA (ng)
1.5×10^6
1×10^6
5×10^5
0
*
HJ SJH SJ
G
NAD+/NADH
Ratio
10
8
6
4
2
0
HJ SJH SJ
H
AMP, ADP, ATP
Ion counts / Total DNA (ng)
6×10^7
4×10^7
2×10^7
0
*
*
*
*
AMP ADP ATP
HJ
SJH
SJ
I
Energy Charge
[ATP]+1/2[ADP] / [ATP] + [ADP] + [AMP]
0.75
0.70
0.65
0.60
0.55
HJ SJH SJ

Supplemental Figure 2

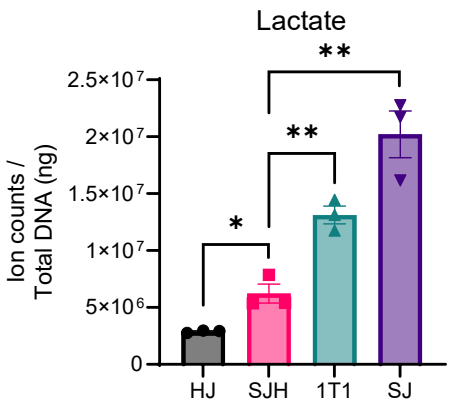

Supplemental Figure 3

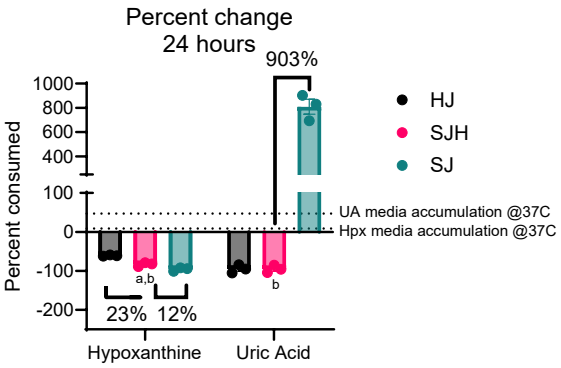

ITUM Pearson Correlation Matrix: SJH vs HJ

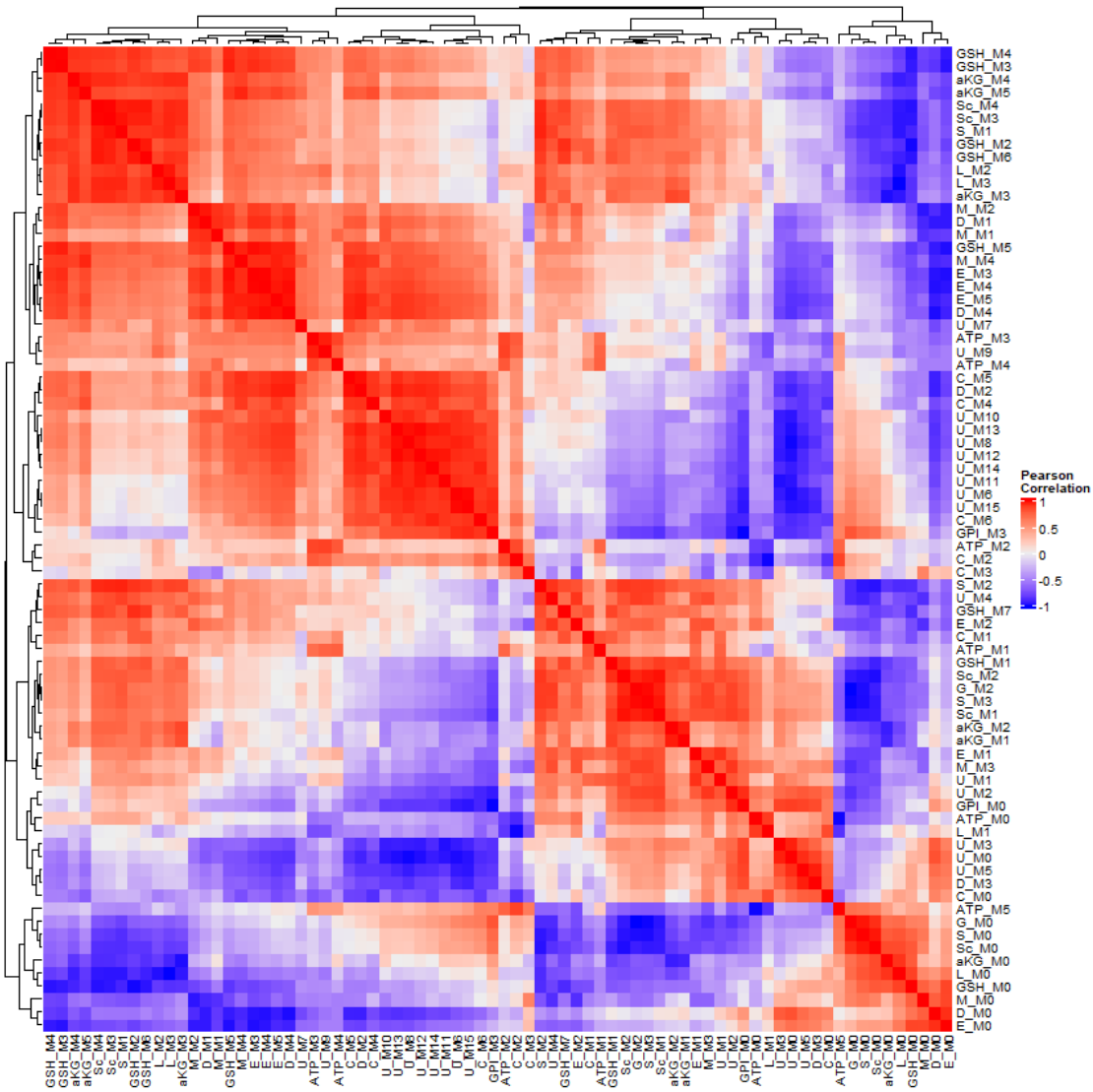

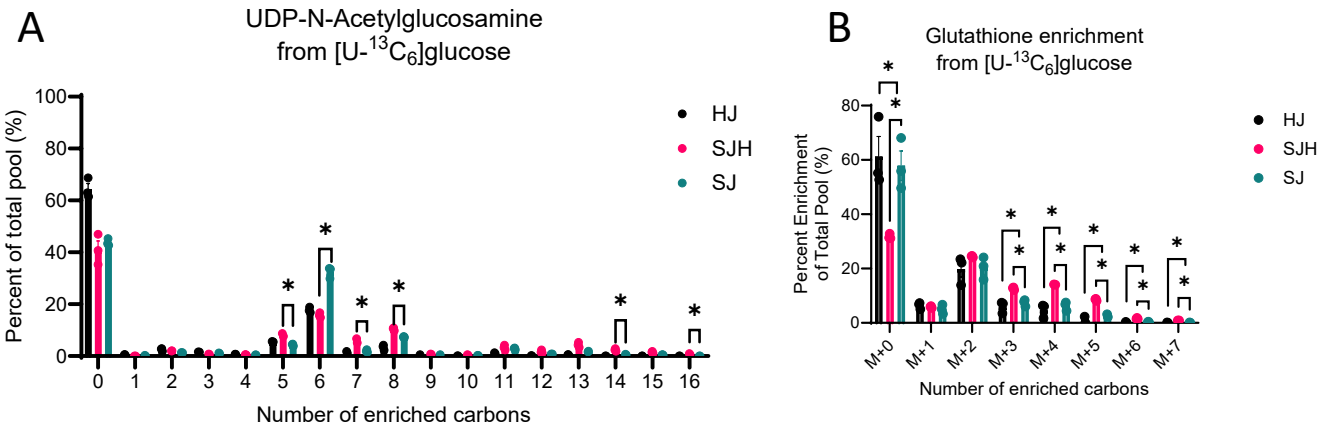
A
UDP-N-Acetylglucosamine
from [U-13C6]glucose
Percent of total pool (%)
100
80
60
40
20
0
0 1 2 3 4 5 6 7 8 9 10 11 12 13 14 15 16
Number of enriched carbons
HJ
SJH
SJ
B
Glutathione enrichment
from [U-13C6]glucose
Percent Enrichment
of Total Pool (%)
80
60
40
20
0
M+0 M+1 M+2 M+3 M+4 M+5 M+6 M+7
Number of enriched carbons
HJ
SJH
SJ

A

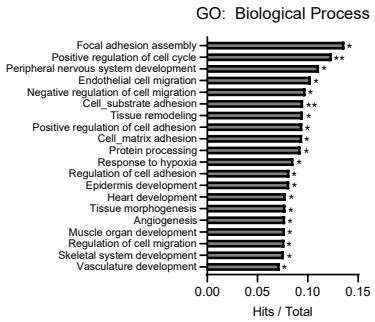
GO: Biological Process
Focal adhesion assembly
Positive regulation of cell cycle
Peripheral nervous system development
Endothelial cell migration
Negative regulation of cell migration
Cell_substrate adhesion
Tissue remodeling
Positive regulation of cell adhesion
Cell_matrix adhesion
Protein processing
Response to hypoxia
Regulation of cell adhesion
Epidermis development
Heart development
Tissue morphogenesis
Angiogenesis
Muscle organ development
Regulation of cell migration
Skeletal system development
Vasculature development
0.00
0.05
0.10
0.15
Hits / Total

B

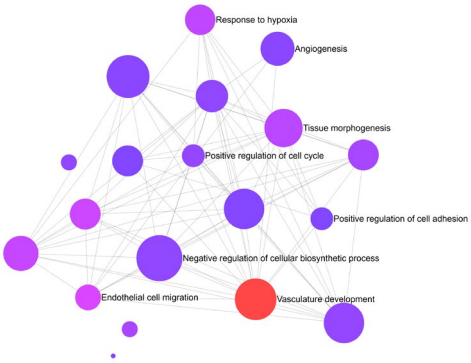
Response to hypoxia
Angiogenesis
Tissue morphogenesis
Positive regulation of cell cycle
Positive regulation of cell adhesion
Negative regulation of cellular biosynthetic process
Endothelial cell migration
Vasculature development